JGR Earth Surface

Key Points:

- We revealed the physical mechanism of submarine landslides initiated from small slip surfaces with different patterns
- We simulated the entire 3D submarine landslide evolution integrating the pre-failure initiation and post-failure mass movement
- We quantified the slip surface growth within a weak layer and its transition into slab failure above the weak layer

Correspondence to:
W. Zhang,
wangcheng.zhang@durham.ac.uk

Author Contributions:
Conceptualization: W. Zhang
Data curation: W. Zhang
Formal analysis: W. Zhang
Investigation: W. Zhang, A. M. Puzrin
Methodology: W. Zhang
Project Administration: A. M. Puzrin
Resources: A. M. Puzrin
Software: W. Zhang
Supervision: A. M. Puzrin
Validation: W. Zhang
Visualization: W. Zhang
Writing – original draft: W. Zhang
Writing – review & editing: A. M. Puzrin

How Small Slip Surfaces Evolve Into Large Submarine Landslides—Insight From 3D Numerical Modeling

W. Zhang[1,2] and **A. M. Puzrin**[2]

[1]Department of Engineering, Durham University, Durham, UK, [2]Institute for Geotechnical Engineering, ETH Zurich, Zurich, Switzerland

Abstract Submarine landslides are a major marine geohazard affecting resilience of offshore infrastructure and coastal urban centers. Attention has previously been paid to quantifying post-failure dynamics of catastrophic submarine debris flows and their consequences. However, pre-failure initiation and growth of a small slip surface evolving into a large submarine landslide are still less understood. This study aims to explore the physical failure mechanism of submarine landslides initiated from small slip surfaces and to quantify key features of failure evolution. They are achieved by modeling the entire three-dimensional (3D) landslide evolution, integrating the initiation and growth of slip surface, failure of slab above the slip surface, post-failure mass movement and re-deposition of transported sediments, using a novel numerical method. The characteristics of the slip surface growth within a favored layer and the patterns of the slab failure in the overlying layer have been thoroughly discussed. The transition from the pre-failure slip surface growth to the diverse post-failure mass movement are first observed and discussed with the 3D geometry effects, revealing the complex cascading mass movement mechanisms. The criterion for unstable growth of a planar slip surface and critical condition for slab failure are proposed. The findings from the study facilitate scientific understanding of the evolution of historic events and help safeguarding offshore developments against submarine landslide recurrence.

Plain Language Summary A submarine landslide can impact a seafloor area as large as over 1,000 km^2 and trigger catastrophic tsunami waves, but originate from a relatively small initiation zone, spreading within a "sandwiched" weak layer. The physical mechanism behind the failure extension is difficult to assess even with the help of state-of-the-art geophysical and geological investigations. To close the knowledge gap, we investigate the entire submarine landslide evolution from the pre-failure initiation to post-failure mass movement using a novel numerical method. From our modeling, we find that the catastrophic growth of a slip surface along a weak layer, together with slab failure extension, could lead to very large submarine landslides. For example, upon certain conditions, a slip surface with an initial size of around only 100 m^2 can grow at considerable speeds and becomes as large as >100 km^2 within minutes. We also reveal key features controlling the development of the slip surface growth and its transition into the slab failure, and hence quantify different phases of failure evolution. The numerical replication of the submarine landslide evolution improves the understanding of the complex cascading mass movement of submarine landslides, and can facilitate safe marine and coastal developments, for example, for offshore renewables.

1. Introduction

Submarine landslides are a major marine geohazard posing significant threats to offshore infrastructure and marine animal habitats, and very large landslides may induce tsunami waves affecting resilience of coastal urban centers. The deadly Papua New Guinea tsunami in 1998 likely caused by a post-earthquake submarine landslide (Tappin et al., 1999) and the Hengchun Slide occurred after earthquakes in 2006, which broke at least nine cables (Lin et al., 2010), are two of the catastrophic events occurred in the past several decades.

Layered marine sediments usually exhibit reduction in strength during shearing, because of the collapse of the inter-particle bonding structures and the accumulation of pore water pressure. The ratio between the initial (peak) and softened (residual) strengths of marine soil sediments is usually between 3 and 7, and such soil with strength sensitive to shearing is referred to as "sensitive soil" (Issler et al., 2015; L'Heureux et al., 2012; Skempton, 1985). For slope failure in marine sensitive soils, shearing failure within a basal slip surface might lead to the growth of the slip surface, eventually evolving into a large translational submarine landslide.
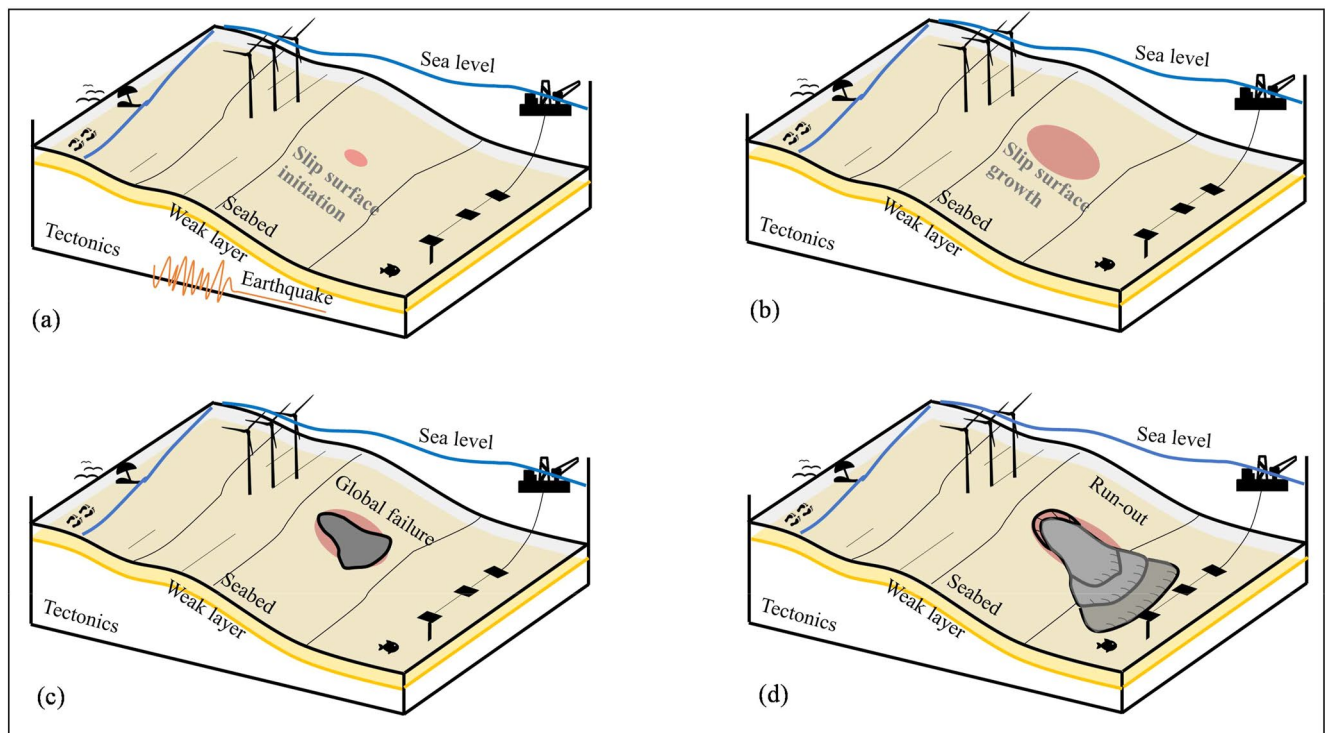
Figure 1. Conceptual evolution of translational submarine landslides: (a) local slip surface initiation in weak layer by triggers such as seismic loading; (b) slip surface growth after triggers; (c) failure of slab above weak layer; (d) post-failure mass movement.

Figure 1 shows a conceptual evolution of typical translational submarine landslides. Although their scales are usually very large, for example, the Storegga Slide involved a total volume of 3,500 km^3 of sediment debris (Haflidason et al., 2004; Micallef et al., 2007), submarine slides might be initiated at a minute slip surface, as shown in Figure 1a, triggered by external factors such as earthquakes. An initial slip surface is often concentrated in a favored soil layer (the so-called 'weak layer") where shear strength relative to the overburden pressure is lower than adjacent layers. The weak layer provides a locus for progressive growth of the slip surface with external triggers (Locat et al., 2014), as shown in Figure 1b. Once the size of the slip surface reaches a threshold, the slip surface growth becomes catastrophic and can only be limited by slope flattening or slab failure above the slip surface (Puzrin et al., 2015, see Figure 1c). Diverse post-failure behavior, such as retrogressive failure with the main rupture surface extending along the upslope direction (Kvalstad et al., 2005) and progressive plowing with continuing erosion of sediments from the seabed by the frontally confined slide mass (Frey-Martínez et al., 2006; Zhang et al., 2021) may evolve after the slab failure, as illustrated in Figure 1d. However, the mechanism of enormous translational landslides evolving from insignificant initial failure, particularly under complex three-dimensional (3D) terrains, remains less understood, which impedes the scientific understanding of historic events and quantification of submarine landslide risks in the future.

Submarine slope stability analysis and assessment of landslide dynamics and impact to offshore infrastructure are important areas of study for engineering geology professionals and geotechnical engineers. Previous studies have treated the pre-failure initiation and post-failure flow dynamics of submarine landslides separately, and no clear vision has been given to the evolution from pre-failure to post-failure phases. Slope stability (failure initiation) is usually simplified as a two-dimensional (2D) plane strain problem (Cornforth, 2005; Morgenstern & Price, 1965; Spencer, 1967), which has been considered conservative compared to the 3D treatment in the Limit Equilibrium Method (LEM), as the resistance in the out-of-plane direction is neglected. However, the slip surface of translational landslides can grow in any direction within a favored "weak" layer, which may or may not be parallel to the main travel direction of the slide mass as depicted in Figure 1. Such a multi-directional propagation mechanism can provide additional driving force because of the reduction in strength during slip surface growth, but this physical failure mechanism cannot be considered in a 2D scenario. A few LEM studies have been able to consider 3D submarine slope stability analysis with rotational sliding mechanisms in the past two decades (Somphong

et al., 2022; Sultan et al., 2007). Zhang et al. (2020) and Klein and Puzrin (2021) studied the instability of 3D submarine slopes with translational sliding mechanisms ignoring inertia effects and considering simplified planar and conical slope geometries, respectively. The robustness of the proposed criteria and their applications in more general conditions need to be validated.

Simulation of the slide mass movement after slab failure has been performed by using sophisticated large deformation numerical methods such as computational fluid dynamics (Biscarini, 2010), smoothed particle hydrodynamics (Zhang & Randolph, 2020) or the material point method (Dong et al., 2017), which are, however, limited to 2D small scale modeling due to computational inefficiency. The depth-integrated method based on the shallow water condition is the most efficient numerical method for the debris flow dynamics modeling pioneered by Imran et al. (2001) and advanced by many following studies (De Blasio et al., 2004; Elverhøi et al., 2005). Some 3D numerical programmes such as Bingclaw (Kim et al., 2019), based on the depth-integrated method, have been emerging recently for modeling dynamics of both slide mass and generated tsunami waves. However, they require prior knowledge of details of the initial slide mass such as geometry, volume and velocity, which are rarely determined in practice with sufficient accuracy. A correlation between slope stability analysis (landslide initiation) and evolved debris flow (landslide dynamics) has been given for a 2D cross-section of a submarine slope (Zhang & Puzrin, 2021). This is yet to be extended to the 3D scenario considering the multidirectional expansion which is essential for fully understanding the failure evolution and more importantly for quantifying impact area and involved volume of a submarine landslide.

Therefore, the main aims and novelty of this study are to reveal how a small slip surface evolves in a 3D geometry (with lateral expansion) into a large submarine landslide, and to quantify its different phases of failure evolution. They are achieved by integrated modeling of pre-failure initiation and post-failure behavior of submarine landslides with 3D geometry effects using a novel numerical method. This numerical method is tested against a historic event occurred on the eastern margin of New Zealand. Key features and controlling factors for the transition from multidirectional slip surface growth within the weak layer to post-failure mass movement are revealed. New criteria for slip surface growth are proposed and characteristics of slab failure are discussed. The findings from the study facilitate scientific understanding of the evolution of historic events and help safeguarding offshore developments against submarine landslide risks.

2. Methods

2.1. Slope Geometry

Four types of submarine slopes (planar, S-shape, convex, and concave, as shown in Figure 2) are used in the study. Each of them consists of a submarine slope, an upper basin floor, and a lower basin floor from nearshore to deep sea. The seabed profile is built of an overlying layer, a weak layer, and a base (undisturbed or less disturbed layers below the weak layer). An initial slip surface was assumed to occur within the weak layer at the center of the slope. The submarine slope is assumed to have an average inclination of 6° to horizontal. Glide planes of submarine landslides are typically up to 10° on the upper slope, reducing to less than 5° on the lower slope (Masson et al., 2006). The S-shape slope used in present study reflects this general trend reducing the slope angle from 9° to nearly 0°. Investigations of slip surface growth and slab failure initiation focus on the planar slope, which is assumed sufficiently long (8,000 m) and wide (6,000 m). The complete landslide evolution, including the post-failure behavior and the arrest of mass transport deposit (MTD), is then simulated with considerations of the full slope model and different 3D slope geometries.

A local Cartesian coordinate system x-y-z is used, with the origin set at the center of the initial slip surface. The x–y plane ($z = 0$) was set as the horizontal plane and the z-axis points away from the seabed as shown in Figure 2. The expression of the planar slope geometry is straightforward with the coordinate z linearly varying from the slope crest to the toe (see Figure 2a). To describe the S-shape slope geometry, a curvilinear slope model was used, where the weak layer is parallel to the slope surface and antisymmetric about the slope center. The slope center is set as the origin of the coordinate system, and the weak layer geometry is described by (see Figure 2b)
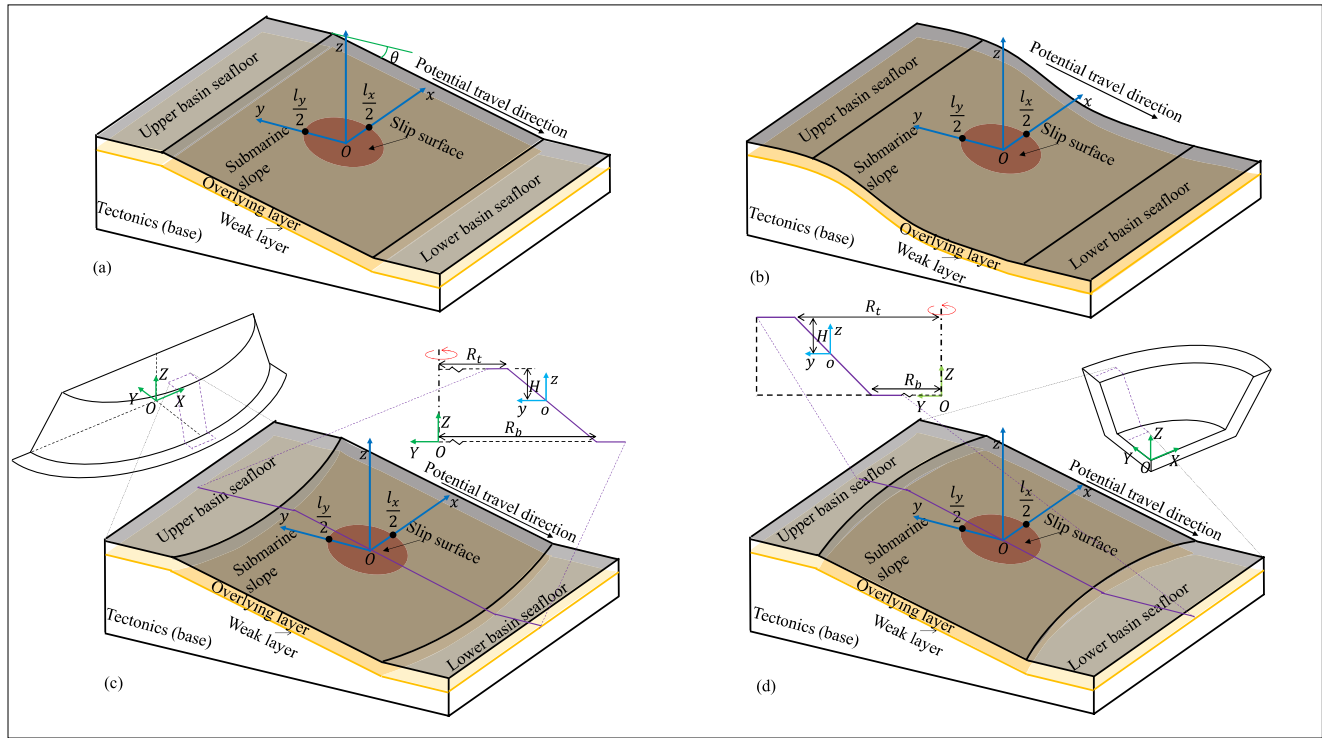
Figure 2. 3D submarine slope models used in the study: (a) planar; (b) S-shape; (c) convex; and (d) concave.

$$z = \begin{cases} -H\left[1 - exp\left(\frac{y}{H}tan\,\theta_c\right)\right], & y < 0 \\ H\left[1 - exp\left(-\frac{y}{H}tan\,\theta_c\right)\right], & y \geq 0 \end{cases} \tag{1}$$

where θ_c is the maximum slope angle at the center, and H is the half-height of the slope. The 3D model is constructed by extending the above function through the x axis.

The convex and concave slope geometries are constructed from a truncated cone and expressed, in terms of a global Cartesian coordinate system X-Y-Z as shown in Figures 2c and 2d, by

$$Z = 2H\left(1 - \frac{\sqrt{X^2 + Y^2} - R_t}{R_b - R_t}\right) \tag{2}$$

and

$$Z = 2H\frac{\sqrt{X^2 + Y^2} - R_b}{R_t - R_b} \tag{3}$$

where R_t and R_b are radii of circular cross sections of the truncated cone through the slope crest and the slope toe, respectively. The local coordinates can then be easily related to the global coordinates based on the origin shifting as shown in Figures 2c and 2d.

2.2. Governing Equations

Key assumptions for establishing governing equations are as follows.

- The thickness of the landslide is small (<1:10) compared to its dimensions, so that the velocity can be averaged along the depth of each cell.
- Momentum of the slide mass along the z-direction is negligible.

- Trapped water moves together with soils in each cell, and any generated pore pressures have no time to dissipate, ensuring an undrained (and incompressible) condition.

Based on these assumptions, conservation of mass in each cell can be expressed by

$$\frac{\partial h}{\partial t} + \frac{\partial hu}{\partial x} + \frac{\partial hv}{\partial y} = 0 \tag{4}$$

where h is the thickness of the slab above the weak layer, u and v are the velocity in the x- and y-directions, respectively, and t is the elapsed time. Conservation of momentum in each cell is given by

$$\frac{\partial hu}{\partial t} + \frac{\partial hu^2}{\partial x} + \frac{\partial h\sigma_x}{\rho \partial x} + \frac{\partial huv}{\partial y} - \frac{\partial h\tau_{xy}}{\rho \partial y} - \frac{\tau_{w,x} + \tau_{g,x} + \tau_{drag,x}}{\rho} = 0 \tag{5}$$

and

$$\frac{\partial hv}{\partial t} + \frac{\partial hv^2}{\partial y} + \frac{\partial h\sigma_y}{\rho \partial y} + \frac{\partial huv}{\partial x} - \frac{\partial h\tau_{xy}}{\rho \partial x} - \frac{\tau_{w,y} + \tau_{g,y} + \tau_{drag,y}}{\rho} = 0 \tag{6}$$

for the x- and y-directions, respectively. In the above equations, ρ is the bulk density of saturated soil, σ_x, σ_y and τ_{xy} are stress components applied at the center of the cell face, with the face normals parallel to the x or y axis; $\tau_{w,x}$ and $\tau_{w,y}$ are weak layer (or slip surface) shear stress components; $\tau_{g,x}$ and $\tau_{g,y}$ are shear stress components at the buried depth of the weak layer by gravity; and $\tau_{drag,x}$ and $\tau_{drag,y}$ are shear stress components by drag of ambient water.

The governing equations are solved through a finite volume scheme with a staggered mesh strategy, which is detailed in Appendix A. Determination and numerical implementation of marine sediment properties and drag forces from the ambient sea water are also fully addressed in Appendix A, with key instructions given as follows. Water entrainment into the slide mass and runout hydroplaning have not been considered at this stage in the study.

2.2.1. Marine Sediment Properties and Drag Force

The soil properties, such as stress and strength, in the weak layer and sliding layer are updated based on the current values of h, u and v. Within the slip surface, the shear stress (τ_w) is limited to the current shear strength, which is reduced during shearing, and given by

$$\tau_w = max \left(1 - \frac{\delta^p}{\delta_r^p}, \quad \frac{1}{S_t} \right) \cdot s_{uw,p} \tag{7}$$

where $\delta^p = \int_0^t \|\dot{\delta}^p\| dt$ is the accumulated plastic shear displacement across the weak layer, δ_r^p the value of δ^p at the residual shear stress, S_t the soil sensitivity defining the ratio of the peak and residual shear strengths, and $s_{uw,p}$ the peak undrained shear strength in the weak layer. Hydrodynamic pressure drag for a streamlined body like a submarine sliding mass is less significant than the skin friction drag, and the latter can be approximated by (Elverhoi et al., 2005; Norem et al., 1990)

$$\tau_{drag} = \frac{1}{2} C_f \rho_w v^2; \ C_f = \left(1.89 + 1.62 \, log \frac{L}{k} \right)^{-2.5} \tag{8}$$

where C_f is the frictional drag coefficient, ρ_w is the seawater density, L is the maximum length of the sliding mass along the travel direction (i.e., y-direction) and k is the roughness length of the sliding mass surface in the range of 0.01–0.1 m (Norem et al., 1990). For a length of the sliding mass varying between 10 and 1,000 m, the friction drag coefficient falls in the range of 0.005–0.016 according to Equation 8. In the present study, the value of k was set to the upper limit 0.1 m, and the value of L is measured from the numerical modeling results. It increases during the submarine landslide evolution.

2.3. Verification

In this section, the developed numerical scheme is tested by modeling a realistic submarine landslide occurred on the eastern continental margin of New Zealand. The landslide was recently discovered and reported by Watson
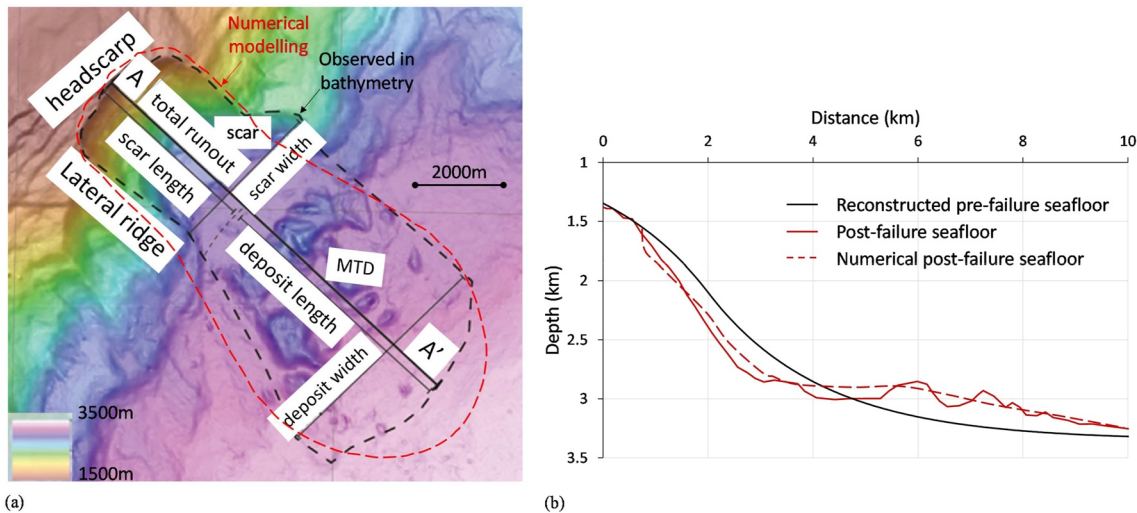
Figure 3. Verification of computational method by modeling a submarine landslide on eastern margin of New Zealand (Watson et al., 2020): (a) top view morphology of the landslide for headscarp, lateral ridge and s; and (b) post-failure slope surface along the cross-section A-A′.

et al. (2020) with clear morphologies of head scarp, lateral ridges and MTD as shown in Figure 3a. The main headscarp is observed around 3,000 m in width and at a water depth of 1,500 m, and the total runout distance from the headscarp to the MTD front is about 10,000 m with the MTD found at a water depth of 3,500 m. The pre-failure slope was reconstructed using the S-shape function with the maximum slope angle $\theta_c = 25°$ and the half-height of the slope $H = 1,250$ m, as shown in Figure 3b. Read from the bathymetry map, the depth of the slip surface, h, is about 100–200 m and was chosen as 150 m in the study. The peak undrained shear strength of the sediments was set to 500 kPa for both the weak layer ($s_{uw,p}$) and the sliding layer ($s_{us,p}$), and the bulk density was set to $\rho = 1,800$ kg/m^3. The soil sensitivity is $S_t = 2$, and the parameter δ_r^p is 0.2 m. The setting of the parameters is to ensure the pre-failure slope is in a marginal state with the undrained shear strength (500 kPa) slightly larger than the shear stress at the steepest point of the slope (497 kPa). The triggering factor of the event is unknown but is likely related to significant seismic activity in the region. Nevertheless, it is reasonable to assume that the failure starts from a small region at the steepest segment of the slope. Here, we assumed a circular initiation zone of 200 m in diameter at the slope center.

The numerical results in terms of the final configurations of the headscarp, lateral ridges and MTDs are visualized in Figure 3a. Figure 3b compares the post-failure seafloor surfaces from the numerical modeling and the bathymetry map adapted from Watson et al. (2020). Compared to the observations from the bathymetry map, the total runout distance is about 10% larger and the headscarp is slightly more extended. The numerical morphology of the landslide is symmetric while it is not the case observed from the bathymetry map, since numerical modeling ignored the heterogeneity of the slope geometry and of the sediment properties along the x axis. Despite that, the results from the numerical modeling compare well with the realistic observations, thus validating the applicability of the proposed numerical scheme to modeling of this 3D large-scale submarine landslide. The mechanisms controlling the propagation of the slip surface along the weak layer, as well as the slab failure and post-failure evolution of submarine landslides similar to the one simulated above will be demonstrated in the remaining of the study.

3. Results

In this section, the numerical results of the whole evolution of submarine landslides are presented covering the initiation and growth of slip surface, slab failure, post-failure evolution and final redeposition of slide mass.
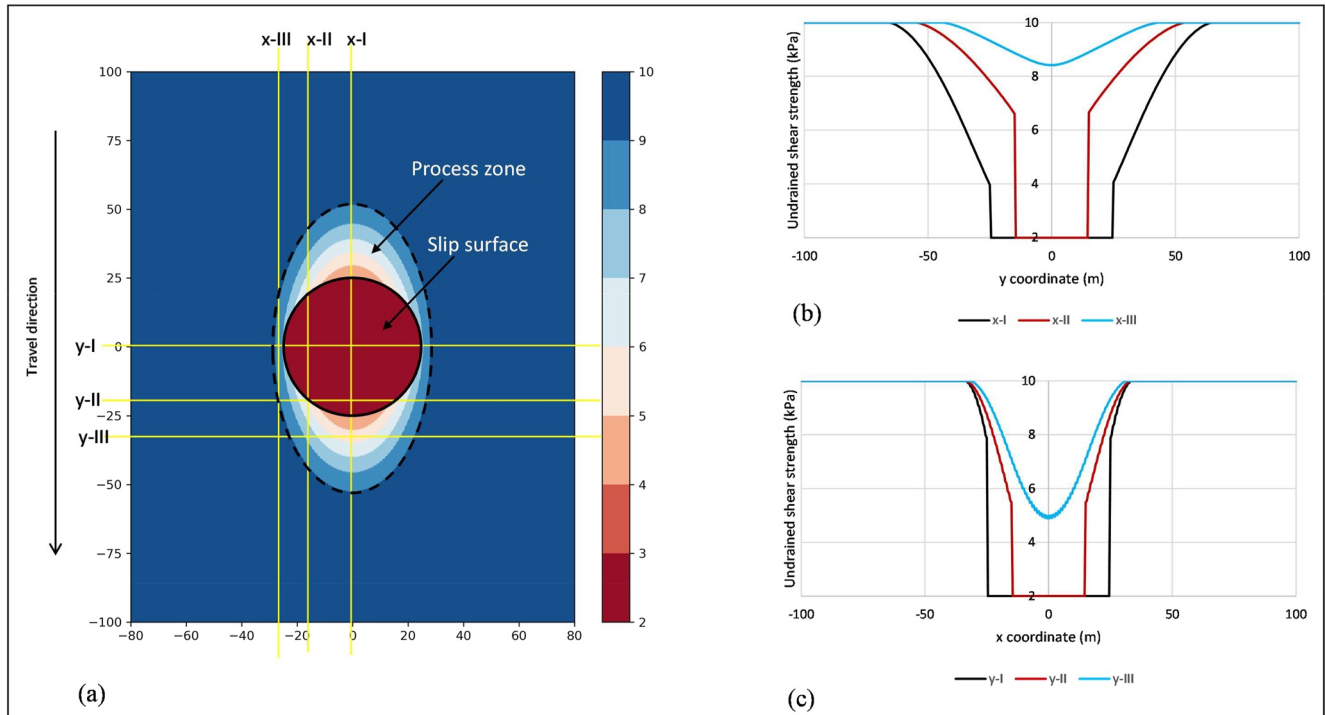
Figure 4. A typical case with stable growth of slip surface: (a) shear strength contour; (b) distributions of shear strength along cross sections parallel to *x*-axis; and (c) distributions of shear strength along cross sections parallel to *y*-axis. Three zones are identified during slip surface growth: slip surface with residual strength (red); intact zone with peak strength (blue); and process zone with reducing strength (band color).

3.1. Initiation of Slip Surface

The initial local slip surface occurs where the permanent or transient driving force exceeds the resistance. It forms either because of an increase in the driving force, for example, by seismic events or increase in slope from diapirism, or a decrease in shear strength, for example, by soil degradation or accumulation of pore pressures. The size and shape of initial slip surface depend on the terrain and triggering factors. In this initial study, it is sufficient to assume the initial slip surface being symmetric with respect to both *x*- and *y*-axis, and its boundary can be described by a series of functions:

$$\left|\frac{2x}{l_x}\right|^n + \left|\frac{2y}{l_y}\right|^n = 1 \tag{9}$$

where *n* is a shape parameter, and l_x and l_y are dimensions of the slip surface in the x- and y- directions, respectively. The value of *n* is larger than unity for a convex slip surface, and for most cases studied here, it was taken as 2 representing for an elliptical or circular slip surface. The sediments within the slip surface are degraded by slip weakening, time weakening or both, although the process may take a long time. Therefore, it is sufficient and conservative to assume that the shear strength in the slip surface has been reduced to the residual.

The force imbalance from the slip surface is transferred and sustained by surrounding soils, which may undergo plastic failure and post-peak strain softening. Figure 4 shows the contour of shear strength after the formation of a circular slip surface ($n = 2$, and $l_x = l_y = 40$ m), as simulated by using the proposed numerical scheme. At the initial state, the shear strength is maintained at the peak value outside the slip surface. The at-rest lateral earth pressure coefficient, which is the ratio between the horizontal and vertical earth pressures, was set to $K_0 = 0.5$. Other properties of the numerical model and materials are listed in Table 1. Within the weak layer, three zones can be identified as shown in Figure 4a: the intact zone (where soils remain intact), the "process zone" (where soils undergo strain softening, and shear strength ranges between the peak and the residual) and the slip surface (where soils reach the residual state). Six cross sections, three in each (*x*- or *y*-) direction, are chosen to further observe the distribution of the shear strength within the three zones, as given in Figures 4b and 4c. For the *x*-I, *x*-II, *y*-I and

Table 1
Base Parameters for Numerical Cases

Parameter	Value	Unit
Overall model length, L	4,000	m
Overall model width, B	150	m
Slope angle, θ	6.0	degrees
Sliding layer thickness, h	8.0	m
Shear stiffness in weak layer, K	1,656	kPa/m
Shear modulus in sliding layer, G	500	kPa
Peak shear strength in weak layer, $s_{uw,p}$	10	kPa
Residual shear strength in weak layer, $s_{uw,r}$	2	kPa
Plastic shear displacement to the residual strength, δ_r^p	0.2	m
Plastic shear strain to the residual strength, $\varepsilon_{s,r}^p$	0.2	
At-rest lateral earth pressure coefficient, K_0	0.5	
Characteristic length[a], l_c	10	m
Submerged soil density, ρ	740	kg/m^3

a$l_c = \sqrt{\dfrac{Gh\delta_r^p}{\tau_p - \tau_r}}$.

y-II sections which cross all three zones, discontinuities in the distributions of the shear strength exist, dropping from a post-peak value to the residual. These distinguish the process zone from the initial slip surface. The x-III and y-III profiles, however, cross the process zone and intact zone only, and the discontinuity in shear strength distribution is absent. Note that, in this case, the process zone is developed to fully resist the unbalanced forces from the slip surface, and hence the slope remains stable. This is defined as stable slip surface growth and will be detailed in the next sub-section.

3.2. Stable Growth of Slip Surface

Figure 5 shows the development of the process zone during stable growth of slip surface. For a relatively large slip surface (i.e., $l_x = 40$ m for a circular slip surface), it can disturb and weaken adjacent soils, forming a significant process zone surrounding the slip surface. However, if the slip surface is sufficiently small (e.g., $l_x = 20$ m), the driving force from the slip surface might be easily sustained by the surrounding soils without the formation of the process zone, that is, the soils remain intact as shown in Figure 5. When the diameter of the slip surface grows to $l_x = 30$ m, the process zone appears only at the front and rear of the slip surface. The above observation reveals that: (a) for a circular slip surface, the process zone first emerges at the rear and in front of the slip surface; and (b) the larger the slip surface, the more significant the process zone. Figure 5 also compares the shear stress contours resulting from different sizes of slip surface. The shear stress is maintained at the value under gravity far away from the slip surface (≈ 6 kPa for parameters listed in Table 1) and increases to the peak at the interface between the intact and process zones. It is limited to the shear strength within the process zone and the slip surface.

Stability can be eventually achieved for the cases of $l_x = 20$, 30 and 40 m despite the development of the process zone. As defined above, the process of extensive expansion of the slip surface up to $l_x = 40$ m can be termed stable slip surface growth. In contrast, for the case of $l_x = 50$ m, the growth of the slip surface cannot be restricted under existing forces and hence is termed unstable slip surface growth. Note that Figure 5 shows a transient
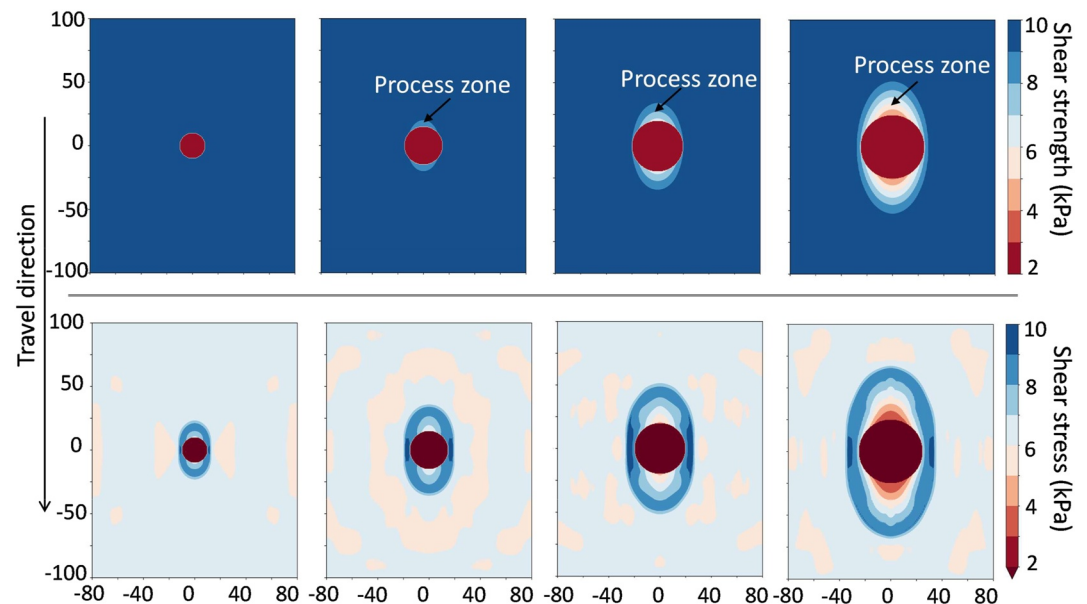

Figure 5. Investigation of stable slip surface growth in terms of the evolutions of shear strength (top row) and shear stress (bottom row) contours. The submarine slope remains stable with the growth of the slip surface up to 40 m in diameter and turns unstable when the diameter reaches 50 m (the last column subfigures show a transient moment).
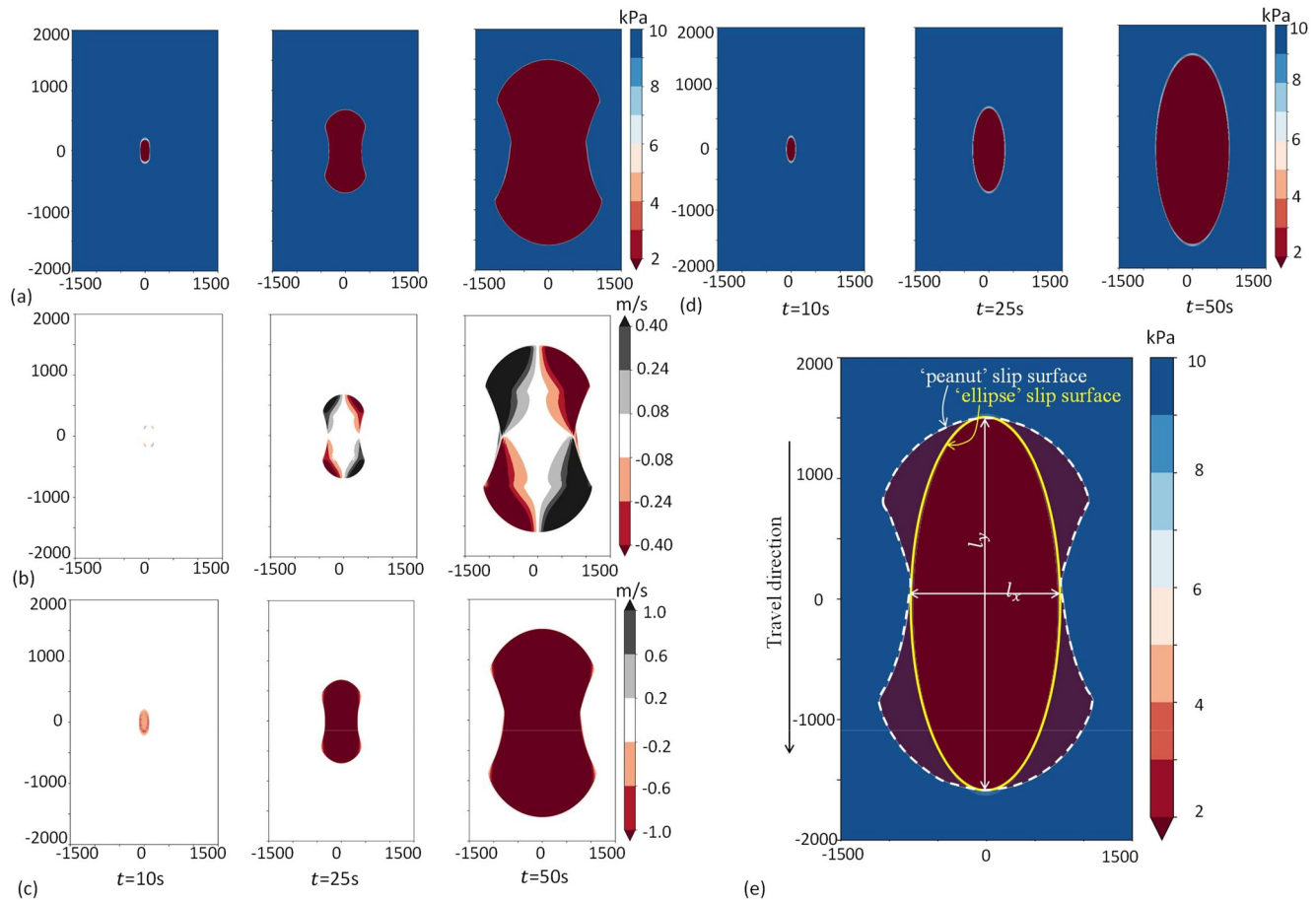
Figure 6. Investigation of unstable slip surface growth from initial diameter of 50 m in terms of evolutions of: (a) shear strength contours, (b) lateral velocity contours and (c) vertical velocity contours for the case of free movement in x direction (perpendicular to the travel direction); (d) shear strength contours for the case of restricted movement in x direction; and (e) a comparison of "peanut" and "ellipse" slip surface growth patterns. (a–c) present information for the case of free movement in x direction showing a "peanut" pattern with more significant lateral expansion at shoulders of the slip surface; and (d) with restricted movement in x direction presents a "ellipse" mechanism.

moment of this case, and the dynamic unstable expansion of the slip surface during unstable slip surface growth will be discussed in the next section. Therefore, in this regard, one may imagine that a circular slip surface gradually expands due to different processes over geologic time until its radius reaches 50 m causing a sudden catastrophic expansion and resulting in a submarine landslide.

3.3. Unstable Growth of Slip Surface

With an initial slip surface of $l_x = l_y = 50$ m and other properties listed in Table 1, the growth of the slip surface is unstable and can only be limited by slope flattening or slab failure. Figures 6a–6c, respectively, shows the evolution of the shear strength contour, horizontal velocity field and vertical velocity field during the unstable growth of the slip surface. To investigate the slip surface growth, the shear strength in the overlying layer was intentionally set to a high value (1,000 kPa) to avoid slab failure. At $t = 10$s, the slip surface grows from a circle to an ellipse with the major axis parallel to the potential travel direction. Thereafter, the slip surface grows dramatically and propagates more outward at the four shoulders, forming a distinctive "peanut" shape at $t = 25$s. The wide shoulders are generated because of larger horizontal velocity in these areas, whereas along the major (y-) and minor (x-) axes of the slip surface, the horizontal velocity is close to zero, as shown in Figure 6b. The slip surface is symmetric in terms of both x- and y-axes before $t = 50$s. At $t = 50$s, however, the downslope part of the slip surface is slightly larger than the upslope, as soil begins to be accumulated more downslope.
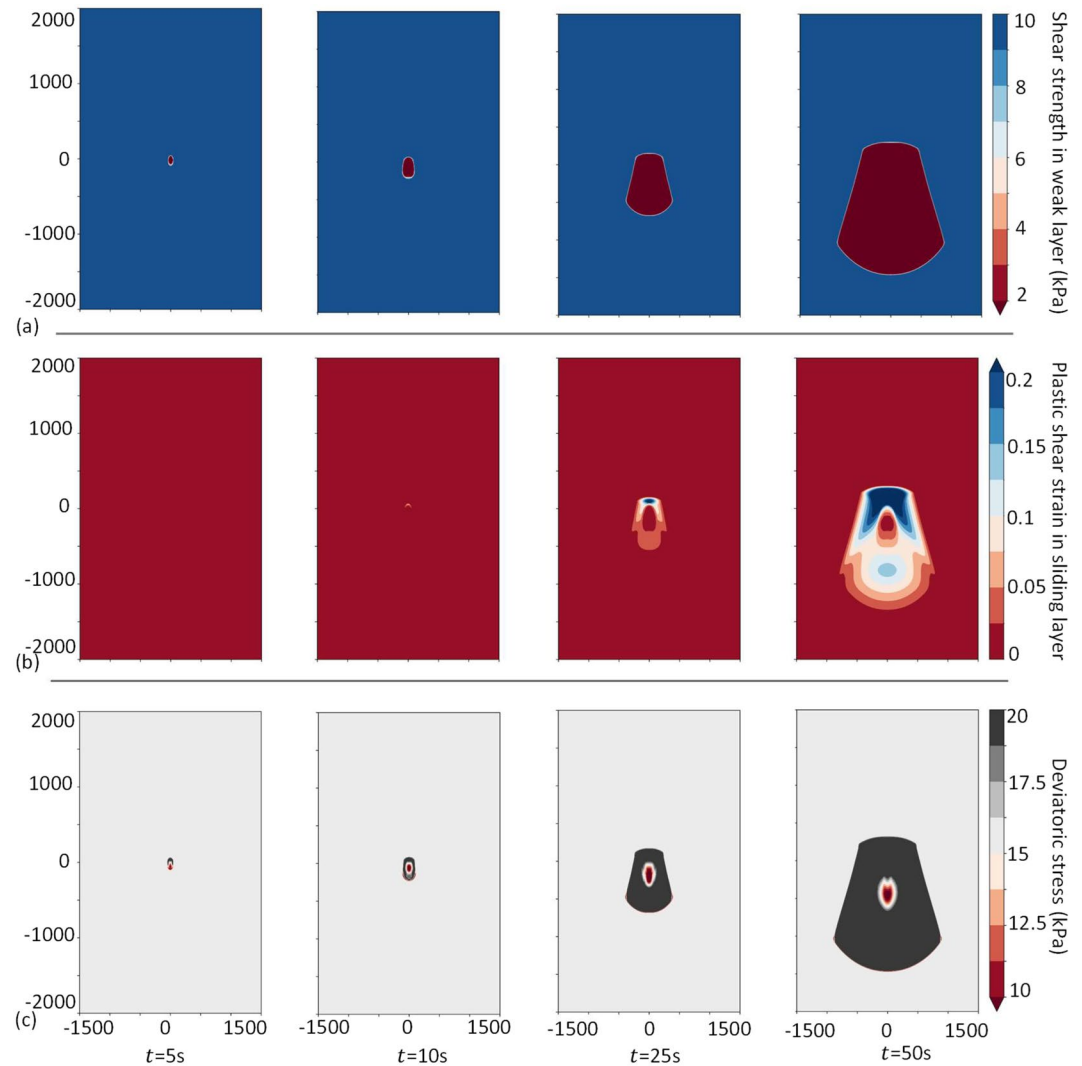
Figure 7. Investigation of slab failure in terms of the evolutions of contours of shear strength in weak layer (top row) and plastic shear strain in sliding layer (bottom row) for the case with $s_{us,p}/s_{uw,p} = 1$ and $K_0 = 0.5$. Note: after slab failure, the slip surface does not grow as a complete "peanut'" with only the lower half developing; the upper half is limited by the headscarp and evolves with the retrogressive failure in this case.

3.3.1. Slab Failure

As stated above, when the peak shear strength in the sliding layer is high, the failure takes place along the weak layer, forming a peanut shaped slip surface. However, when the peak shear strength was reduced to $s_{uw,p} = s_{us,p} = 10$ kPa, unstable slip surface growth resulted in a slab failure. Figure 7 shows the contours of the plastic strain and von Mises stress in the overlying layer, together with the continuing slip surface growth in the weak layer during slab failure. The von Mises stress (see its expression in Appendix A) is often used to determine if a given material experiences plastic flow. At $t = 5$ s, slab failure emerges at the rear of the slip surface where soils are unloaded and the stress reaches the maximum 20 kPa; while in front of the slip surface, soils are loaded and the stress decreases from the initial value. At $t = 10$ s, the soils in front of the slip surface have been loaded to the (passive) failure state, and, accordingly, the stress reaches the maximum. Thereafter, the slab failure propagates mainly at the downslope portion with diffusive plastic strain; at the rear of the slip surface, the plastic strains are accumulated, but the propagation of the slab failure is not apparent. Instead of the fan zone formed in front of the slip surface, the rear boundary of the slip surface (or the main scarp) is quite straight to slightly arcuate. For the planar slope studied here, the slip surface keeps growing along the x-direction, with the side boundaries of the slip surface continuing to extend further outward.
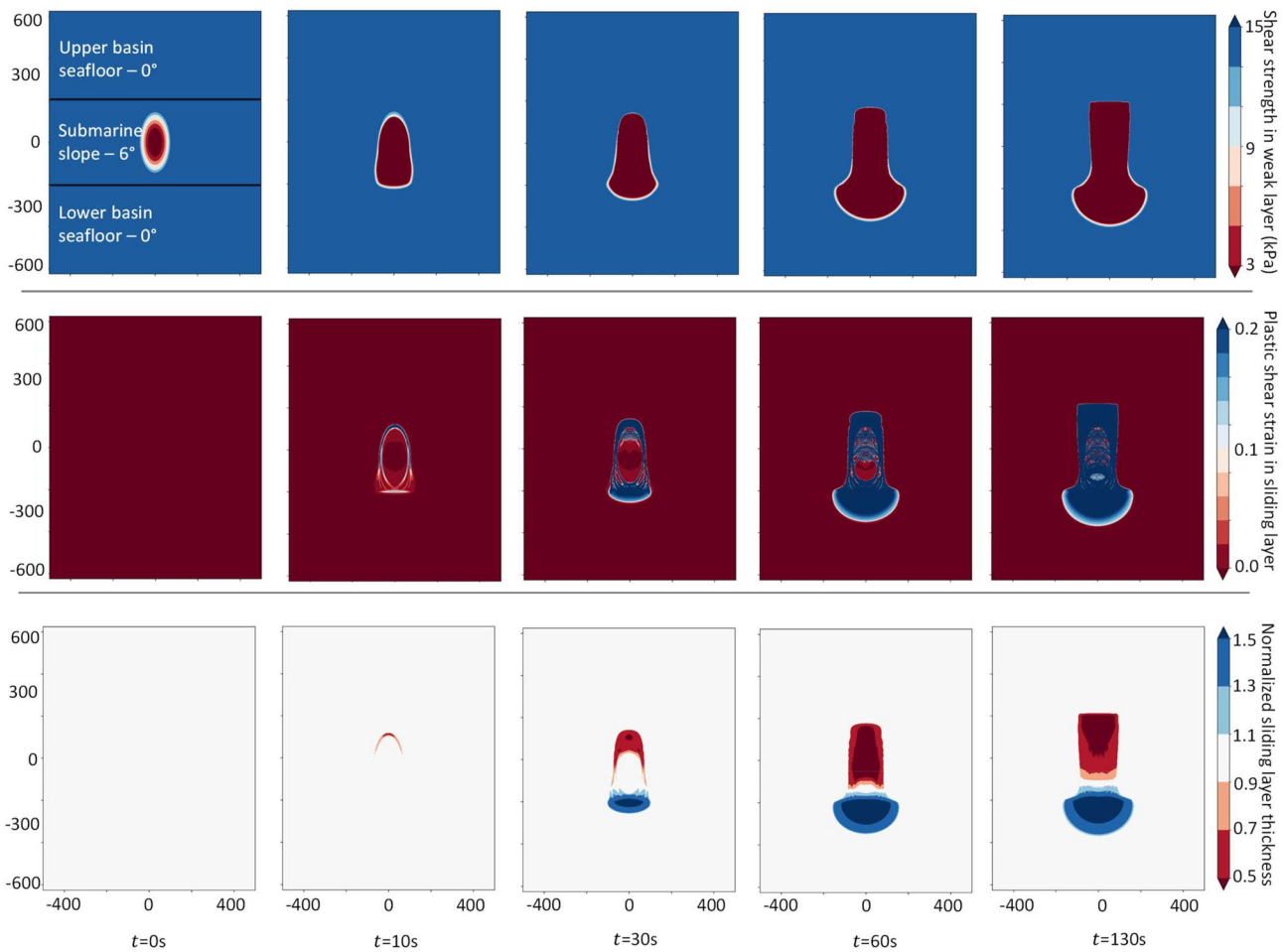
Figure 8. Investigation of post-failure mass movement in terms of the evolutions of contours of shear strength in weak layer (top row), plastic shear strain in sliding layer (middle row) and normalized sliding layer thickness (bottom row). Slab failure initiates at upper slope followed by formation of an intact detached block and disintegration with traveling; mass transport deposits (MTDs) are found at lower basin forming a fan.

3.4. Post-Failure Evolution and Redeposition of Slide Mass

It has been demonstrated above that, once initiated, the slip surface growth and slab failure extension cannot be arrested on a planar slope. Either slope flattening or material strengthening can restrict slip surface growth and slab failure extension. To further observe the arrest of slip and post-failure behavior, the full model including flat basin floors at the margins of the submarine slope, as shown in Figure 2, is used. It consists of a submarine slope with a slope angle of 6° and length of 400 m (coordinate y from −200 to 200 m), an upper basin floor ($y < −200$ m) and a lower basin floor ($y > 200$ m). The peak shear strength of the weak layer soil, the weak layer depth and the submerged soil unit weight were chosen as $s_{uw,p} = 15$ kPa, $h = 8$ m, and $\gamma' = 8$ kN/m³, respectively. This parameter set generates a strength ratio of $s_{uw,p}/\gamma' h = 0.234$, which is typical for normally consolidated marine sediments. The overlying layer was assumed slightly over-consolidated with a peak strength of $s_{us,p} = 10$ kPa and strength ratio of 0.31. The soil sensitivities of the weak layer and the overlying layer were set to 7 and 2, respectively. An elliptical initial slip surface of $l_x = 40$ m and $l_y = 80$ m was pre-set. Other parameters are the same as those listed in Table 1.

Figure 8 shows the landslide dynamic evolution from the slab failure initiation, post-failure stage to re-deposition with respect to the contours of the shear strength in the weak layer and the plastic strain in the overlying layer, and the changes in the overlying layer thickness. Note that the normalized sliding layer thickness is calculated as the ratio of the current thickness and the initial thickness of the overlying layer. At $t = 10$ s, slab failure is initiated with a certain amount of slip surface growth. The failure is more concentrated at the rear of the slip surface, and

a curved back scarp is formed at this stage, with the height of the scarp exceeding 4 m ($0.5h$). The main scarp moves backward with the retrogressive failure at the rear of the slip surface. The retrogression is stopped by the flat upper basin floor, leaving a straight main scarp of 200 m in length and over 4 m in height. Because of the material degradation, the failed overlying mass is torn apart into blocks, as shown in the second row of Figure 8. The blocks are broken into smaller pieces and finally disappear during their downward movement. The failed and softened slide mass is finally deposited at the lower basin floor, forming a compressed fan zone of around 400 m in diameter and over 4 m in thickness. The extent of the slip surface in the weak layer is almost identical to the combined area of the source region and deposition fan zone.

4. Discussion

4.1. Mechanism and Evolution of Translational Submarine Landslides

Observed from the numerical modeling, the evolution of translational submarine landslides can be summarized as follows.

1. *Slip surface initiation.* A slip surface might be formed and grow stably within a weak layer due to external triggers such as earthquakes and excess pore pressure accumulation. Strain softening of sensitive soils during shearing leads to the formation of a process zone, where shear strength reduces from the peak toward the residual, surrounding the slip surface.
2. *Slip surface growth.* Once the slip surface reaches a certain size, its growth becomes unstable and catastrophic, restricted by slope flattening or slab failure only. The critical area of the slip surface for unstable growth is almost independent of its shape but depends on the material properties and shear stress at the slip surface. Regardless of the initial shape, the slip surface transitions from an ellipse to a "peanut" pattern during the unstable growth stage.
3. *Slab failure.* With the growth of the slip surface, the driving force increases. Therefore, at a certain stage of the unstable slip surface growth, the overlying soils may reach the maximum allowable stress, initiating slab failure. After the slab failure, the growth of the slip surface is in alignment with the propagation of the slab failure.
4. *Post-failure evolution.* A main scarp forms at the rear of the slip surface after the slab failure, and is followed by retrogression, which is limited by slope flattening. The failed slide mass disintegrates into blocks and then turns to fully softened debris flow with downward movement. The slide mass finally re-deposits at the lower basin with the MTDs forming a fan zone.

4.2. Features of Dynamic Slip Surface Evolution

4.2.1. Slip Surface Growth Pattern

The pattern of stable growth of the slip surface depends on the shape of the initial slip surface. Figure 9 shows the different growth patterns for elliptical slip surfaces with different ratios of major and minor axes, in terms of the shear strength contour. In all cases, the stable growth of the slip surface together with the development of the process zone is obvious. As demonstrated above, for a circular slip surface with $l_x/l_y = 1$, the travel direction (x-direction) is the favored direction for slip surface growth. This is enhanced with a larger axis ratio (a wider slip surface), for example, $l_x/l_y = 2$. For a slender slip surface (of small axis ratio, $l_x/l_y = 1/3$), however, the slip surface tends to propagate along the y-direction first, presenting a different growth pattern from wide slip surfaces. For instance, with $l_x = 20$ m and $l_y = 60$ m, soil at the two sides of the slip surface begins to fail while the soil in front and at the rear of the slip surface remains intact. With the axis ratio $l_x/l_y = 1/2$, the slip surface seems to grow simultaneously along the periphery of the slip surface without an obvious favored direction, which forms the most pessimistic situation.

The growth of the slip surface along the x-direction is driven by the compression force downslope and extension force upslope, akin to the in-plane shear mode of crack propagation in fracture mechanics (i.e., a shear stress acting parallel to the plane of the slip surface and perpendicular to the slip surface front); while the growth along the y-direction is driven by shearing, akin to the out-of-plane shear mode of crack propagation in fracture mechanics (i.e., a shear stress acting parallel to the plane of the slip surface and parallel to the slip surface front). Here, the former is defined as the compression-extension mode and the latter is defined as the shear mode. A combined mode including both the compression-extension and shear modes is expected to be more common,
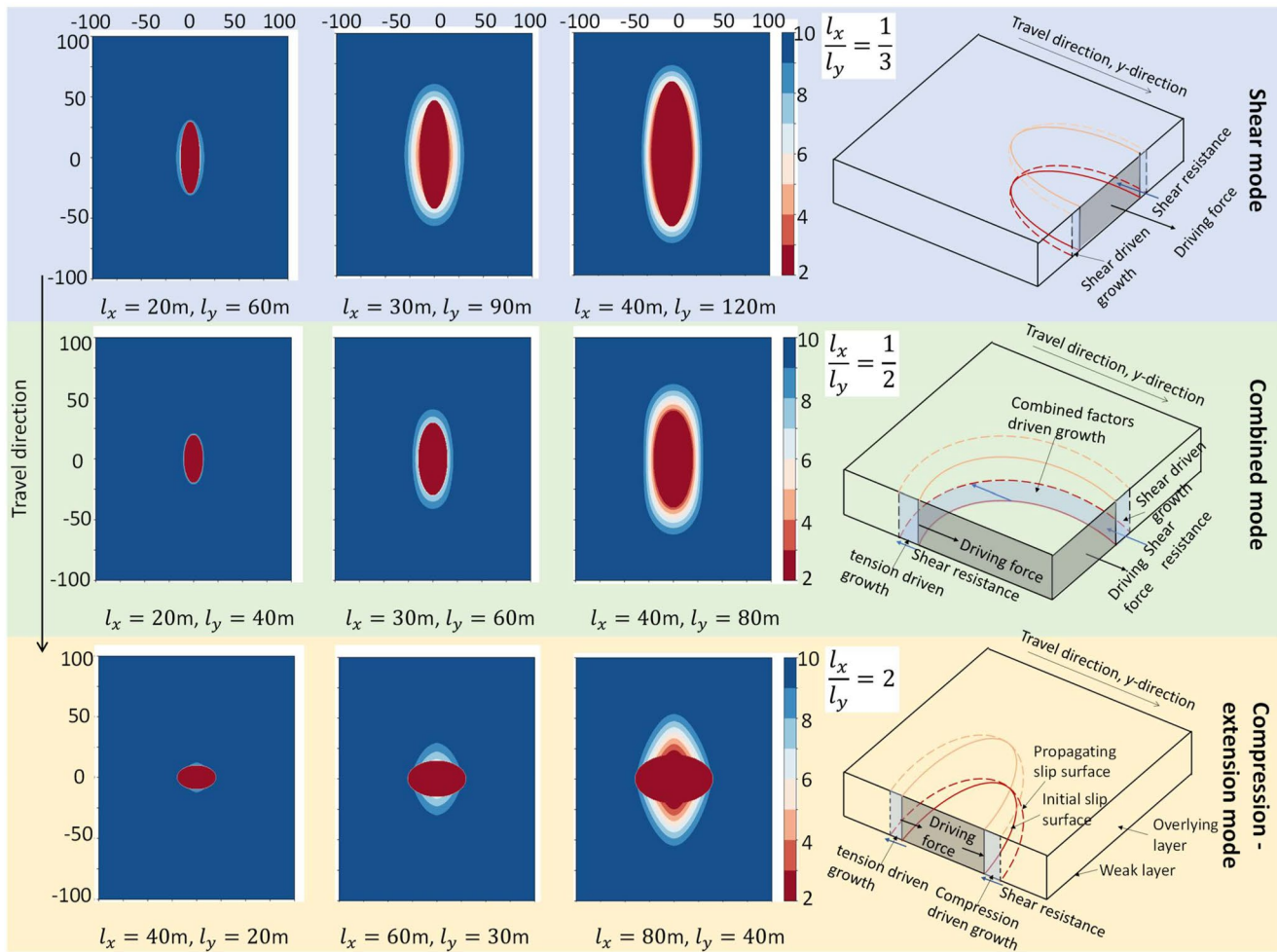
Figure 9. Three modes of initial slip surface growth: the shear mode (top row) with lateral expansion favored; the compression—extension mode (bottom row) with upslope and downslope expansion; and the combined mode (middle row) with expansion in all directions.

particularly when the slip surface growth is unstable and continuous. The mechanisms for different growth modes have been conceptually illustrated in Figure 9. It has not been possible to study the shear and combined modes in previous 2D investigations (e.g., Kvalstad et al., 2005; Puzrin et al., 2004; Zhang et al., 2015).

Zhang et al. (2020) assumed that the (horizontal) velocity of the slide mass along the x- direction is negligible compared to the y-direction component, which generates a plane strain condition with the compression/extension modulus in the sliding layer calculated by

$$E_{ps} = \frac{E}{1 - \nu^2} = \frac{2G}{1 - \nu} \tag{10}$$

where E is the Young's modulus and ν the Poisson's ratio. Though this assumption has proved to be not physically true for the stage of unstable slip surface growth as shown in Figure 6b, it would be helpful to investigate its effect on slip surface growth and hence determine if it is sufficient for analytical analysis. To achieve this, conservation of momentum in the x-direction, that is, governing Equation 5, was ignored and the horizontal component of the velocity was set to zero. Numerical results of such an idealized case in terms of the strength contours are presented in Figure 6d. For $t = 5$ s and 10 s, the slip surfaces of the idealized case are almost identical to the case formulated by rigorous governing equations as shown in Figure 6a. However, with further unstable growth of the slip surface, the shape of the slip surface remains an ellipse, as opposed to the "peanut" shape of the rigorous case. Figure 6e compares the two mechanisms at $t = 50$ s. The major and minor axes of the "peanut" slip surface are the same as those of the "ellipse" slip surface, with the area of the slip surface larger in the former mechanism.

The different mechanisms found in the two cases imply that the horizontal movement of the slide mass plays an important role and must be considered during the unstable growth of the slip surface.

4.2.2. Slip Surface Growth Speed

Once a slip surface falls into the unstable growth stage, the growth speed depends on how the unbalanced forces are transferred within the overlying layer. For the compression-extension mode, the growth of the slip surface is driven by the compressional/tensile force, and therefore the growth speed (of the major axis) can be related to the compression wave velocity

$$v_{maj} = 2\sqrt{\frac{E'}{\rho}} \tag{11}$$

where E' is the compression modulus. Note that the number 2 in the expression means that the growth speed is double the wave velocity, as the slip surface grows in both the upslope and downslope directions. Similarly, for the shear mode, the growth speed of the minor axis can be related to the shear wave velocity

$$v_{min} = 2\sqrt{\frac{G}{\rho}} \tag{12}$$

For plane strain and undrained conditions, the compression modulus, $E' = E_{ps,}$ is four times the shear modulus (see Equation 10) and therefore, the major axis always doubles the minor axis of the slip surface. This can be seen in Figure 6e, where the major axes of the slip surfaces are almost 3,000 m while the minor axes are around 1,500 m in both mechanisms.

Figure 10a shows the length (major axis) and width (minor axis) of the slip surface during its growth for the selected case, compared with the analytical solutions given by Equations 11 and 12. It should be noted that the growth of the slip surface evolves from the stable to unstable stages with the transition emerging at around $t = 4$ s. During the stable growth stage, both axes of the slip surface are assumed unchanged. With this idealization, the growth of the two axes of the slip surface in the numerical modeling can be well predicted by the analytical solutions, with the growth speeds being 34 m/s and 68 m/s for the minor and major axes, respectively. Such fast speeds reveal that unstable growth of the slip surface is catastrophic and significantly differs from creep failure.

Figure 10b gives the area of the slip surface during its unstable growth for both mechanisms. For the "ellipse" mechanism, the area can be calculated exactly by

$$A = \frac{\pi}{4} l_x l_y \tag{13}$$

which is shown by the good agreement between the numerical and analytical results in the figure. The area of the ellipse slip surface is initially 1,962.5 m^2 and increases to 3.6 km^2 in 50 s. The peanut slip surface (5.3 km^2 calculated from the numerical modeling results) is about 45% larger than the ellipse slip surface at $t = 50$ s. The fast growth of the slip surface implies that during an earthquake, even with a short period of shaking, a large slip surface with a magnitude of several km^2 might be formed. Such a large slip surface may further result in slab failure and debris flow. Therefore, it is key to determine in what conditions the slip surface can grow unstably, which will be discussed in the next sub-section.

4.3. Criteria for Unstable Growth of Slip Surface

For a slip surface described by a series of functions Equation 9, the area of the slip surface can be calculated by

$$A = \frac{l_x l_y}{n} \cdot \frac{\Gamma(1 + 1/n)\Gamma(1/n)}{\Gamma(1 + 2/n)} \tag{14}$$

where Γ is the gamma function. By integrating the normal and shear resistances along the boundary of the slip surface, one may calculate the total resistance and compare it to the driving force from the slip surface, whereby the critical area of the slip surface for unstable growth is given by Zhang et al. (2020)

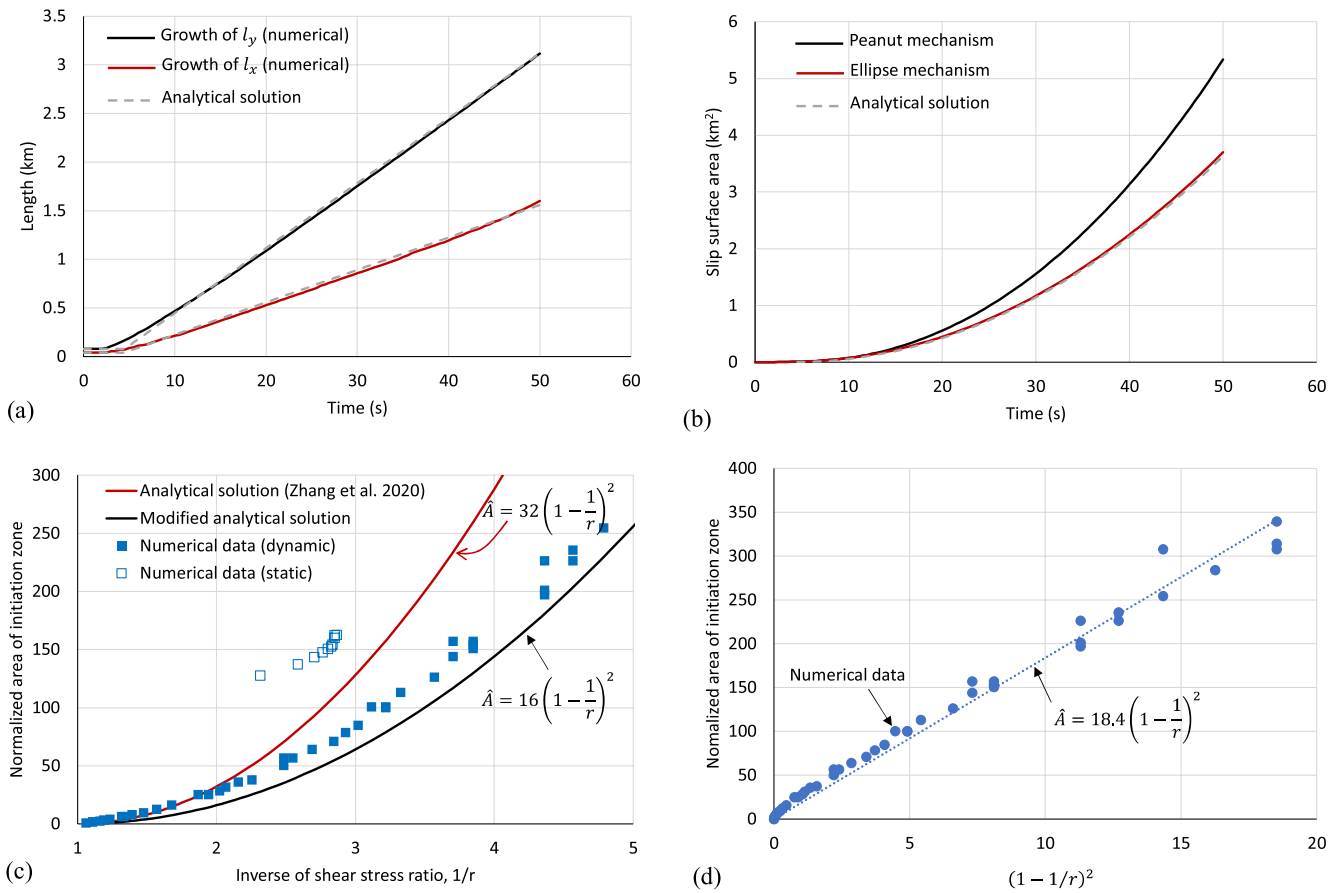$$A_{cri} = 32\left(\frac{1-r}{r} l_c\right)^2 \tag{15}$$

Figure 10. Speed of slip surface growth in terms of (a) lengths of major and minor axes and (b) area of slip surface; (c) critical area of slip surface for unstable growth by numerical and analytical analyses; and (d) best fitting of numerical data.

where r is the shear stress ratio and l_c is the characteristic length relevant to the process zone size, given by

$$r = \frac{\tau_g - s_{uw,r}}{s_{uw,p} - s_{uw,r}}, \; l_c = \sqrt{\frac{Gh\delta_r^p}{s_{uw,p} - s_{uw,r}}} \tag{16}$$

For static analysis, ignoring any inertia effects, the Equation 15 is conservative compared to the numerical data from finite element and finite difference modeling (Zhang et al., 2020). However, this should be verified under dynamic conditions which can be achieved using the proposed numerical modeling.

A parametric study was conducted to observe the effects of the shape parameter, n, and the dimensions of the slip surface on the critical area for unstable slip surface growth. The gravity loads and the critical surface areas at critical conditions for all cases are presented in Table 2. Figure 10c shows a comparison of the numerical results with or without inertia effects and the analytical results by Equation 15. With inertia effects, the critical area estimated by Equation 15 is not always conservative, particularly with a large shear stress ratio. If the dynamic criterion meets the same series of functions as the static Equation 15, the best fit of the numerical data from the dynamic analysis gives

$$A_{cri} = 18.4 \left(\frac{1-r}{r} l_c \right)^2 \tag{17}$$

which is shown in Figure 10d. This means that the critical area of the slip surface for unstable slip surface growth under dynamic conditions is on average 42.5% smaller than that ignoring inertia effects. This echoes the finding by Zhang et al. (2016) that for a 2D cross-section of a planar slope, the critical length (major axis) of slip surface for catastrophic propagation can be up to 50% lower with inertia effects than without inertia effects. Extending

Table 2
Critical Conditions for Unstable Slip Surface Growth by Numerical Analysis

Dimension of slip surface				Gravity load	
l_x (m)	l_y (m)	n	A (m^2)	ρ (kg/m^3)	r
First series: $l_y/l_x = 1$, $n = 2$					
10	10	2	79	1,170	0.943
20	20	2	314	1,070	0.841
40	40	2	1,257	870	0.637
60	60	2	2,827	730	0.494
80	80	2	5,027	640	0.403
100	100	2	7,854	580	0.341
120	120	2	11,310	540	0.301
140	140	2	15,394	500	0.260
160	160	2	20,106	470	0.229
180	180	2	25,447	450	0.209
200	200	2	31,416	430	0.189
Second series: $l_y/l_x = 2$, $n = 2$					
10	20	2	157	1,130	0.902
20	40	2	628	980	0.749
40	80	2	2,513	750	0.515
60	120	2	5,655	630	0.392
80	160	2	10,053	550	0.311
100	200	2	15,708	500	0.260
120	240	2	22,619	460	0.219
140	280	2	30,788	430	0.189
Third series: $l_y/l_x = 3$, $n = 2$					
10	30	2	236	1,090	0.862
20	60	2	942	910	0.678
40	120	2	3,770	680	0.443
60	180	2	8,482	570	0.331
80	240	2	15,080	500	0.260
100	300	2	23,562	460	0.219
120	360	2	33,929	430	0.189
Fourth series: $l_y/l_x = 0.5$, $n = 2$					
20	10	2	157	1,130	0.902
40	20	2	628	990	0.760
80	40	2	2,513	770	0.535
120	60	2	5,655	640	0.403
160	80	2	10,053	560	0.321
200	100	2	15,708	510	0.270
240	120	2	22,619	470	0.229
280	140	2	30,788	450	0.209
Fifth series: $l_y/l_x = 2$, $n = 1$					
20	40	1	400	1,040	0.811
40	80	1	1,600	830	0.596
60	120	1	3,600	700	0.464

Table 2
Continued

Dimension of slip surface				Gravity load	
l_x (m)	l_y (m)	n	A (m^2)	ρ (kg/m^3)	r
80	160	1	6,400	610	0.372
100	200	1	10,000	550	0.311
120	240	1	14,400	510	0.270
Sixth series: $l_y/l_x = 2$, $n = 10$					
20	40	10	789	950	0.719
40	80	10	3,154	720	0.484
60	120	10	7,097	590	0.352
80	160	10	12,617	520	0.280
100	200	10	19,715	470	0.229
120	240	10	28,389	440	0.199

this observation to the 3D case, one may simply assume for the dynamic unstable growth a 50% reduction in the critical area of the slip surface from the static Equation 17, that is

$$A_{cri} = 16\left(\frac{1-r}{r}l_c\right)^2 \tag{18}$$

Figure 10c shows that Equation 18 gives estimates of the critical slip surface area well below the numerical data and is therefore conservative.

4.4. Effects of a 3D Slope Geometry

Three typical 3D slope types, as shown in Figures 2b–2d, are considered in this section in order to gain an initial insight into the slope geometry effects on the translational landslide evolution. For the S-shape slope, the half-height of the slope in Equation 1 was set to be the same as for the planar slope, that is, $H = 21$ m, and the maximum slope angle was taken as $\theta_c = 9°$ such that the average slope angle within the range of -500 m $< y < 500$ m is equal to the planar slope angle of $6°$. For the convex slope, the values of R_t and R_b were set to 800 m and 1,200 m, respectively; while for the concave slope, $R_b = 800$ m and $R_t = 1,200$ m. The slope angle of the convex and concave slope models is the same with the planar slope model.

Figure 11 compares the final states of the four slope models with respect to the fields of the shear strength in the weak layer, the shear stress in the weak layer, the plastic strain in the sliding layer, and the normalized sliding layer thickness. It can be noted that the far field gravity shear stress fields (second row of Figure 11) strongly depend on the geometry of the problem. The results of the planar, convex and concave slopes look very similar, with slightly more horizontal slip surface growth observed in the convex slope and slightly more retrogressive extension pertained in the concave slope, suggesting that the slope gradient along the x-direction has limited influence on the landslide evolution. In contrast, the final slip surface and MTD observed in the S-shape curvilinear slope are significantly different from the other three models with less extended retrogressive failure and a smaller fan heave zone. This indicates that the slope gradient along the y-direction has a considerable effect on the landslide evolution.

The examples shown here present an initial investigation of 3D post-failure behavior of submarine landslides. Detailed investigation of the effects of the 3D slope geometry on post-failure patterns is beyond the scope of the present work and will be explored in future studies by using the proposed numerical tool.
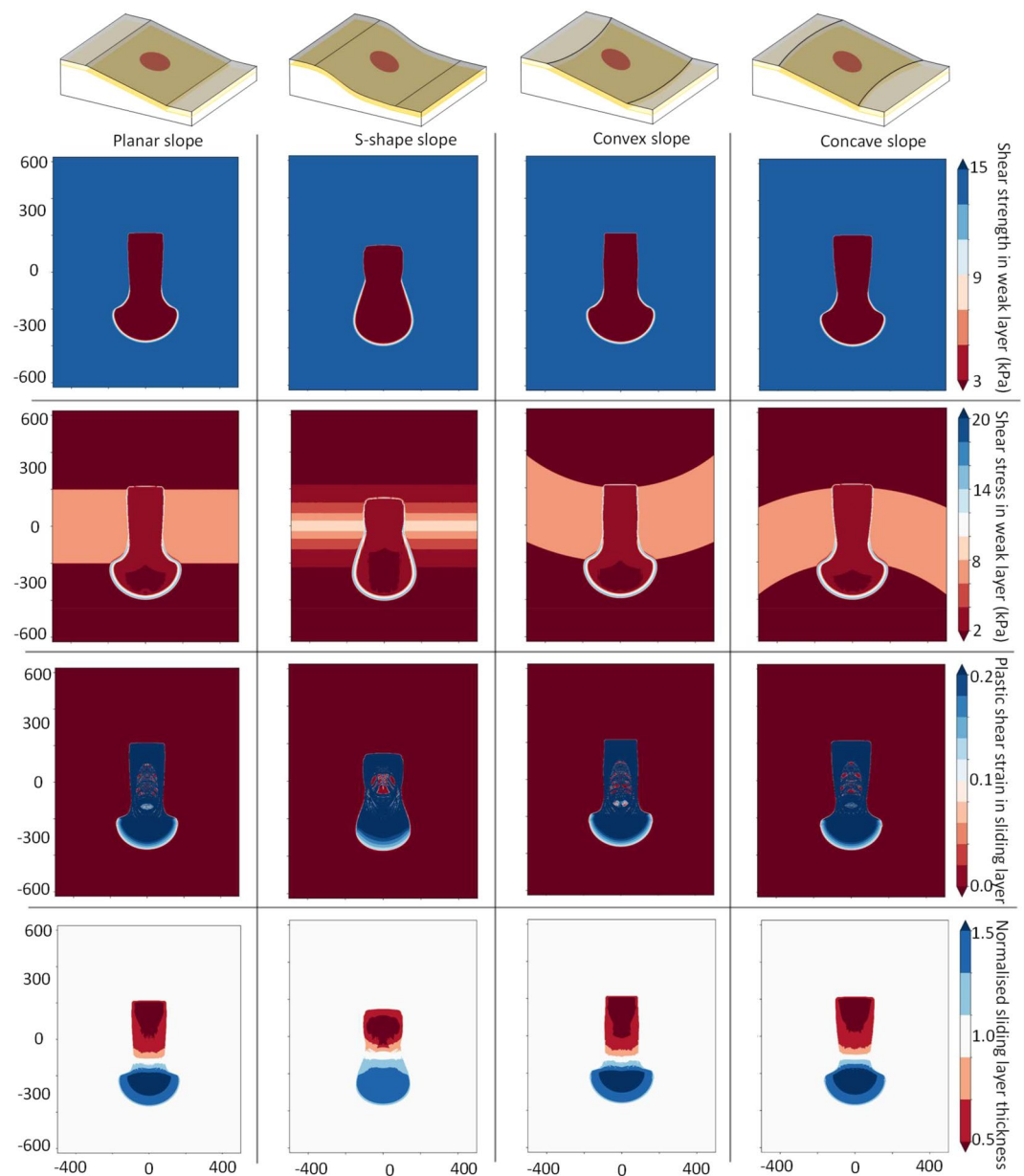
Figure 11. 3D slope geometry effects on the ultimate slip surface growth and morphology of the mass transport deposit (MTD) in submarine landslides in terms of: slope geometry (first row); shear strength in weak layer (second row); shear stress in weak layer (third row); plastic shear strain in sliding layer (forth row); and (d) normalized sliding layer thickness (fifth row). Note: four types of slope geometries—planar (first column), S-shape (second column), convex (third column) and concave (forth column)—are studied with details given in Figure 2; shear strength in weak layer reflects slip surface configuration; plastic strain in sliding layer reflects the intactness of slide mass; normalized thickness is calculated as current thickness over initial thickness.

5. Conclusions

Submarine landslides are a major marine geohazard posing significant threats to offshore infrastructure and coastal urban centers. This study has provided insights into the entire evolution of submarine landslides in three dimensional (3D) slopes by using an original large deformation computational tool. For the first time, the paper combines within a single framework the modeling of both pre-failure initiation and post-failure evolution of 3D submarine landslides. This facilitates understanding of the physical mechanisms behind the development of an enormous submarine landslide from a small slip surface and helps to quantify different stages of the failure evolution.

The findings from the study may advance scientific understanding of historic events and help safeguarding offshore developments against submarine landslide risks.

The complete evolution of submarine translational landslides includes the slip surface initiation and growth along a weak layer, slab failure, post-failure mass movement and re-stabilization, as depicted in Figure 1. A slip surface might be formed with a relatively small size and grow in a stable manner due to external triggers such as earthquakes and excess pore pressure accumulation. The growth pattern depends on the shape of initial slip surface. For an initially wide slip surface, the process zone first emerges in front and at the rear of the slip surface, whereas for an initially slender slip surface, it occurs at the two sides. For an elliptical slip surface, the process zone develops around the periphery of the slip surface without any favored direction. The critical area of the slip surface for unstable growth is almost independent of its shape but depends on the material properties and shear stress ratio over the slip surface. For planar submarine slopes, it is given by $A_{\text{cri}} = 16 \left(\frac{1-r}{r} l_{\text{c}} \right)^2$ where the shear stress ratio, r, and characteristic length, l_{c}, are expressed by Equation 16.

Regardless of the initial shape, the slip surface transitions from an ellipse to a "peanut" pattern during the unstable growth stage, with expansion rates equal to compression wave velocity and shear wave velocity along the major and minor axes of the slip surface, respectively. The slab failure usually initiates at the rear of the slip surface if the horizontal earth pressure is smaller than the vertical one, which is usually the case in submarine sediments. The stronger the overlying layer, the larger the slip surface before the slab failure. A main scarp forms at the rear of the slip surface after the slab failure, and is followed by retrogression, which is limited by upslope slope flattening. Once slab failure is triggered, slip surface growth is controlled by upslope retrogression and downslope plowing, and hence its shape deviates from a "peanut." The slide mass finally re-deposits at the flat terrain with the MTD forming a fan zone. The differences in the landslide failure extension and MTD morphology between the planar, the convex, and the concave slopes of the same and uniform slope angle and parallel layering characteristic of sediments were found to be insignificant. In contrast, in the curvilinear slope, a significantly less extended failure upslope and a smaller fan heave zone downslope have been observed.

Appendix A: Numerical Scheme for 3D Modeling of Submarine Landslide Evolution

The domain of interest, that covers the source and MTD areas of a submarine landslide, is essentially divided into regularized cells, with each cell holding characteristics of the evolving landslide. The edges of the cell are parallel to the axes of coordinates x and y, and the x–y plane ($z = 0$) was set as the horizontal plane and crossing through a reference point (taken as the slope center in the study) at the basal slip surface. Cells are fixed during the landslide process, with materials traveling through them, forming a Eulerian framework. Conservations of mass and momentum are then formulated within each cell, and global instability can be modeled by integrating all cells with consideration of proper inter-cell constitutive models and fluxes.

Conservation of mass in each cell can be expressed by

$$\frac{\partial h}{\partial t} + \frac{\partial hu}{\partial x} + \frac{\partial hv}{\partial y} = 0 \tag{A1}$$

where h is the thickness of the slab above the weak layer, u and v are the velocity in the x- and y-directions, respectively, and t is the elapsed time. Conservation of momentum in each cell is given by

$$\frac{\partial hu}{\partial t} + \frac{\partial hu^2}{\partial x} + \frac{\partial h\sigma_x}{\rho \partial x} + \frac{\partial huv}{\partial y} - \frac{\partial h\tau_{xy}}{\rho \partial y} - \frac{\tau_{w,x} + \tau_{g,x} + \tau_{drag,x}}{\rho} = 0 \tag{A2}$$

and

$$\frac{\partial hv}{\partial t} + \frac{\partial hv^2}{\partial y} + \frac{\partial h\sigma_y}{\rho \partial y} + \frac{\partial huv}{\partial x} - \frac{\partial h\tau_{xy}}{\rho \partial x} - \frac{\tau_{w,y} + \tau_{g,y} + \tau_{drag,y}}{\rho} = 0 \tag{A3}$$

for the x- and y-directions, respectively. In the above equations, ρ is the bulk density of saturated soil, σ_x, σ_y and τ_{xy} are stress components applied at the center of the cell face, with the face normals parallel to the x or y axis; $\tau_{\text{w},x}$ and $\tau_{\text{w},y}$ are weak layer (or slip surface) shear stress components; $\tau_{\text{g},x}$ and $\tau_{\text{g},y}$ are shear stress components,

associated with the gravity, at the buried depth of the weak layer; and $\tau_{\mathrm{drag},x}$ and $\tau_{\mathrm{drag},y}$ are shear stress components associated with the drag of ambient water.

A1. Stress Components at Cell Face Center

Usually, the stress tensor ($\boldsymbol{\sigma}$) describing the stress status at the center of the cell face can be decomposed into

$$\boldsymbol{\sigma} = \boldsymbol{s} + p \cdot \boldsymbol{I} \tag{A4}$$

where $\boldsymbol{s}$ is the deviatoric stress tensor, p the mean stress and $\boldsymbol{I}$ the second-order identity tensor. Note that the vertical normal stress component σ_z can be expressed by

$$\sigma_z = \frac{1}{2} \gamma' h \tag{A5}$$

where $\gamma' = \rho' g$ is the submerged unit weight of soils with ρ' being the submerged density.

Similarly, the strain tensor ($\boldsymbol{\varepsilon}$) can be decomposed into

$$\boldsymbol{\varepsilon} = \boldsymbol{e} + \frac{\varepsilon_v}{3} \cdot \boldsymbol{I} \tag{A6}$$

where $\boldsymbol{e}$ is the deviatoric strain tensor and ε_{v} the volumetric strain. It can also be divided into the elastic and plastic portions, which will be denoted by superscripts 'e' and 'p', respectively, in the remainder of the paper. Note that the volumetric strain satisfies $\varepsilon_{\mathrm{v}} = \varepsilon_{\mathrm{v}}^{\mathrm{e}} = \varepsilon_{\mathrm{v}}^{\mathrm{p}} \to 0$, as the undrained condition was maintained and the von Mises yield criterion with an associated flow rule was used. Hence, one may write $\boldsymbol{\varepsilon} \cong \boldsymbol{e}$, $\boldsymbol{\varepsilon}^{\mathrm{e}} \cong \boldsymbol{e}^{\mathrm{e}}$, and $\boldsymbol{\varepsilon}^{\mathrm{p}} \cong \boldsymbol{e}^{\mathrm{p}}$. The elasticity of materials is assumed linear and isotropic, and therefore the deviatoric stress tensor is expressed by

$$\boldsymbol{s} = 2G\boldsymbol{e}^e \cong 2G\boldsymbol{\varepsilon}^e \tag{A7}$$

where G is the shear modulus.

A modified von Mises yield criterion was adopted in order to consider isotropic and linear strain softening, given by

$$q = max\left(1 - \frac{\varepsilon_s^p}{\varepsilon_{s,r}^p}, \quad \frac{1}{S_t}\right) \cdot 2s_{us,p} \tag{A8}$$

where $q = \sqrt{\frac{3}{2}} \|\boldsymbol{s}\|$ is the von Mises stress, $s_{\mathrm{us,p}}$ the peak undrained shear strength in the sliding layer which can be measured from a triaxial element test; $\varepsilon_{\mathrm{s}}^{\mathrm{p}} = \int_0^t \sqrt{\frac{2}{3}} \|\dot{\boldsymbol{e}}^{\mathrm{p}}\| dt$ the accumulated von Mises strain; $\varepsilon_{\mathrm{s,r}}^{\mathrm{p}}$ the value of $\varepsilon_{\mathrm{s}}^{\mathrm{p}}$ to the residual shear strength; S_{t} the soil sensitivity defining the ratio of the peak and residual shear strengths. $\varepsilon_{\mathrm{s,r}}^{\mathrm{p}}$ can be determined from a triaxial test by $\varepsilon_{\mathrm{s,r}}^{\mathrm{p}} = \frac{2}{3} \gamma_{\mathrm{r}}^{\mathrm{p}}$ where $\gamma_{\mathrm{r}}^{\mathrm{p}}$ is the plastic shear strain associated to the residual undrained shear strength.

A2. Shear Stress at Weak Layer

Within the slip surface, the shear stress (τ_{w}) is limited to the current shear strength, which is reduced during shearing, and given by

$$\tau_w = s_{uw}(\delta^p) = max\left(1 - \frac{\delta^p}{\delta_r^p}, \quad \frac{1}{S_t}\right) \cdot s_{uw,p} \tag{A9}$$

where $\delta^{\mathrm{p}} = \int_0^t \|\dot{\boldsymbol{\delta}}^{\mathrm{p}}\| dt$ is the accumulated plastic shear displacement across the weak layer, $\delta_{\mathrm{r}}^{\mathrm{p}}$ the value of δ^{p} at the residual shear stress, and $s_{\mathrm{uw,p}}$ the peak undrained shear strength in the weak layer. Ignoring displacement beneath the weak layer (Zhang et al., 2015), the horizontal slide displacement can be related to the shear displacement across the weak layer by $\frac{u}{\cos\theta} = \delta = \delta^{\mathrm{e}} + \delta^{\mathrm{p}}$ where θ is the slope angle and δ^{e} and δ^{p} the elastic and plastic portion of the shear displacement, respectively.

Soils surrounding the slip surface are first mobilized elastically before reaching the yield stress governed by Equation A9, and the shear stress is increased to be larger than the initial value caused by gravity. Considering a linear and isotropic elasticity model, the pre-peak shear stress can be expressed by

$$\tau_w = K\delta^e \tag{A10}$$

where K is the shear stiffness.

A3. Finite Volume Scheme

Two layers of fixed meshes with the same mesh size and alignment were taken, as shown in Figure A1a, with the top layer used for solving mass and momentum conservation equations and the bottom layer tracking the changes in soil properties in the weak layer during slip surface growth. A finite volume method with staggered grids, as shown in Figure A1b, was used to integrate and solve the governing Equations A1 to A3.

Let us consider a slope of a rectangular space domain $\Omega : (0, L_x) \times (0, L_y)$ and a time interval $(0, T)$. Dirichlet boundary conditions, that is, $u = 0$ and $v = 0$, are prescribed representing unaffected remote regions. The space domain is meshed with a grid of $N_x \times N_y$ cells, and the cells of dimensions Δx and Δy are indexed by (i, j) where $i \in (0, N_x)$ and $i \in (0, N_y)$. The centers of the bottom, top, left, and right edges of the cell (i, j) are denoted by $\left(i, j - \frac{1}{2}\right), \left(i, j + \frac{1}{2}\right), \left(i - \frac{1}{2}, j\right)$, and $\left(i + \frac{1}{2}, j\right)$, respectively. The mass conservation is integrated and solved over the cell, with the thickness of the sliding layer, h, and slope angle (topography), θ, discretized at the cell center. The velocity in the x-direction is discretized at the center of the edges normal to the x-direction, while the velocity in the y-direction is discretized at the center of the edges normal to the y-direction. The approximation of h at cell (i, j) and time t^n is denoted by $h^n_{i,j}$. The approximation of u at the edge $\left(i + \frac{1}{2}, j\right)$ and time t^n is denoted by $u^n_{i+\frac{1}{2},j}$ while the approximation of v at the edge $\left(i, j + \frac{1}{2}\right)$ and time t^n is denoted $v^n_{i,j+\frac{1}{2}}$.
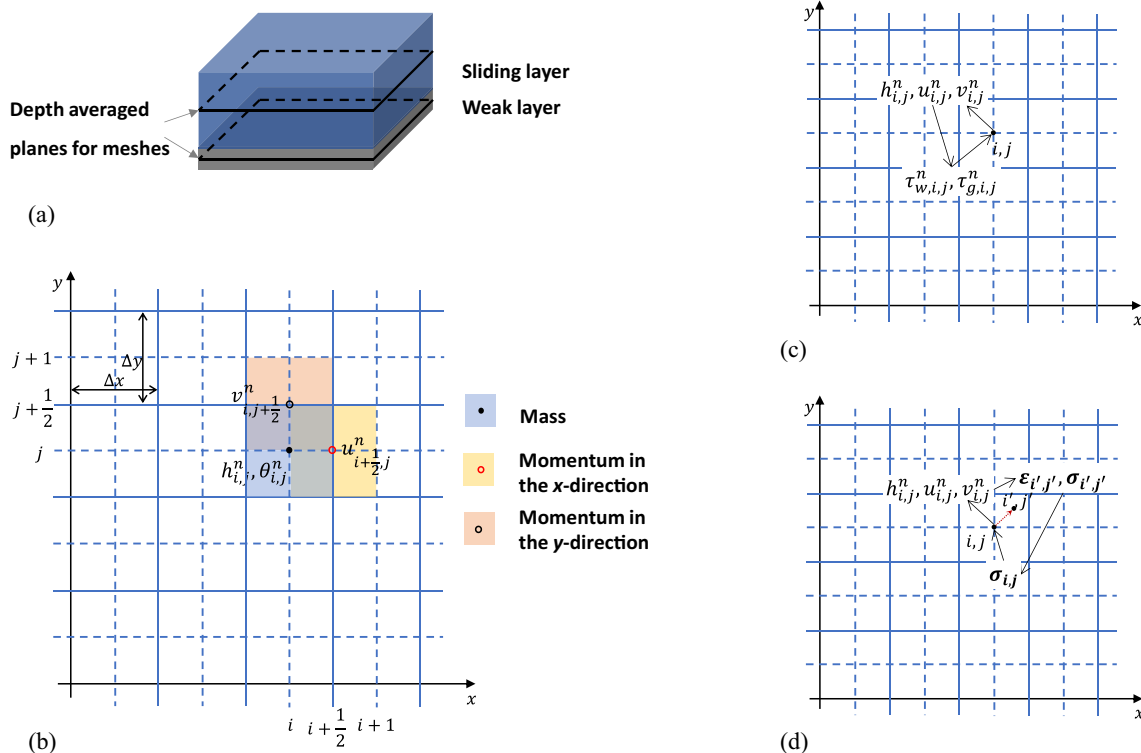

Figure A1. (a) Schematics of depth integrated model; (b) staggered mesh scheme; (c) update of properties for the fixed weak layer; and (d) update of properties for the movable sliding layer.

At time t^{n+1}, the mass conservation Equation A1 is discretized as

$$h_{i,j}^{n+1} - h_{i,j}^n = \frac{\Delta t}{\Delta x}\left(qx_{i-\frac{1}{2},j}^n - qx_{i+\frac{1}{2},j}^n\right) + \frac{\Delta t}{\Delta y}\left(qy_{i-\frac{1}{2},j}^n - qy_{i+\frac{1}{2},j}^n\right) \tag{A11}$$

where

$$qx_{i-\frac{1}{2},j}^n = \hat{h}_{i-\frac{1}{2},j}^n u_{i-\frac{1}{2},j}^n, \quad \hat{h}_{i-\frac{1}{2},j}^n = \begin{cases} h_{i,j}^n & u_{i-\frac{1}{2},j}^n \le 0 \\ h_{i-1,j}^n & u_{i-\frac{1}{2},j}^n > 0 \end{cases};$$

$$qy_{i,j-\frac{1}{2}}^n = \hat{h}_{i,j-\frac{1}{2}}^n v_{i,j-\frac{1}{2}}^n, \quad \hat{h}_{i,j-\frac{1}{2}}^n = \begin{cases} h_{i,j}^n & v_{i,j-\frac{1}{2}}^n \le 0 \\ h_{i,j-1}^n & v_{i,j-\frac{1}{2}}^n > 0 \end{cases} \tag{A12}$$

The momentum conservation in the x-direction, that is, Equation A2, is discretized as

$$
\begin{aligned}
h_{i+\frac{1}{2},j}^{n+1} u_{i+\frac{1}{2},j}^{n+1} &- h_{i+\frac{1}{2},j}^n u_{i+\frac{1}{2},j}^n \\
&= \frac{\Delta t}{\Delta x}\left(qx_{i,j}^n \hat{u}_{i,j}^n - qx_{i+1,j}^n \hat{u}_{i+1,j}^n\right) \\
&+ \frac{\Delta t}{\Delta y}\left(qy_{i+\frac{1}{2},j-\frac{1}{2}}^n \hat{u}_{i+\frac{1}{2},j-\frac{1}{2}}^n - qy_{i+\frac{1}{2},j+\frac{1}{2}}^n \hat{u}_{i+\frac{1}{2},j+\frac{1}{2}}^n\right) \\
&+ \frac{\Delta t}{\rho\Delta y}\left(\tau_{xy,i+\frac{1}{2},j+\frac{1}{2}}^n h_{i+\frac{1}{2},j+\frac{1}{2}}^n - \tau_{xy,i+\frac{1}{2},j-\frac{1}{2}}^n h_{i+\frac{1}{2},j-\frac{1}{2}}^n\right) \\
&+ \frac{\tau_{w,i+\frac{1}{2},j}^n + \tau_{g,i+\frac{1}{2},j}^n + \tau_{drag,i+\frac{1}{2},j}^n}{\rho}
\end{aligned} \tag{A13}
$$

where

$$h_{i+\frac{1}{2},j}^n = \frac{h_{i,j}^n + h_{i+1,j}^n}{2};$$

$$qx_{i,j}^n = \frac{qx_{i-\frac{1}{2},j}^n + qx_{i+\frac{1}{2},j}^n}{2}, \quad \hat{u}_{i,j}^n = \begin{cases} u_{i+\frac{1}{2},j}^n & qx_{i,j}^n \le 0 \\ u_{i-\frac{1}{2},j}^n & qx_{i,j}^n > 0 \end{cases};$$

$$qy_{i+\frac{1}{2},j-\frac{1}{2}}^n = \frac{qy_{i,j-\frac{1}{2}}^n + qy_{i+1,j-\frac{1}{2}}^n}{2}, \quad \hat{u}_{i+\frac{1}{2},j-\frac{1}{2}}^n = \begin{cases} u_{i+\frac{1}{2},j}^n & qy_{i+\frac{1}{2},j-\frac{1}{2}}^n \le 0 \\ u_{i+\frac{1}{2},j-1}^n & qy_{i+\frac{1}{2},j-\frac{1}{2}}^n > 0 \end{cases}; \tag{A14}$$

$$
\begin{aligned}
\tau_{xy,i+\frac{1}{2},j+\frac{1}{2}}^n & h_{i+\frac{1}{2},j+\frac{1}{2}}^n \\
&= \frac{\tau_{xy,i,j}^n h_{i,j}^n + \tau_{xy,i+1,j}^n h_{i+1,j}^n + \tau_{xy,i,j+1}^n h_{i,j+1}^n + \tau_{xy,i+1,j+1}^n h_{i+1,j+1}^n}{4}
\end{aligned}
$$

The momentum conservation in the y-direction, that is, Equation A3, can be discretized in a similar way.

Data Availability Statement

Modeling for this research was conducted using an open-source Python package developed by the first author and available at https://github.com/geotechzhang/TranSliM. The solver has been validated against a historic event occurred on the eastern margin of New Zealand (Watson et al., 2020) with satisfying outcomes. Data used in this study is publicly available at the Figshare repository https://doi.org/10.6084/m9.figshare.17029700.

References

Biscarini, C. (2010). Computational fluid dynamics modelling of landslide generated water waves. *Landslides*, *7*(2), 117–124. https://doi.org/10.1007/s10346-009-0194-z

Cornforth, D. H. (2005). *Landslides in practice: Investigation, analysis and remedial/preventative options in soils*. John Wiley and Sons Inc.

De Blasio, F. V., Engvik, L., Harbitz, C. B., & Elverhøi, A. (2004). Hydroplaning and submarine debris flows. *Journal of Geophysical Research*, *109*(C1), C01002. https://doi.org/10.1029/2002jc001714

Dong, Y., Wang, D., & Randolph, M. F. (2017). Runout of submarine landslide simulated with material point method. *Procedia Engineering*, *175*, 357–364. https://doi.org/10.1016/j.proeng.2017.01.045

Elverhøi, A., Issler, D., De Blasio, F. V., Ilstad, T., Harbitz, C. B., & Gauer, P. (2005). Emerging insights into the dynamics of submarine debris flows. *Natural Hazards and Earth System Science*, *5*, 633–648. https://doi.org/10.5194/nhess-5-633-2005

Frey-Martínez, J., Cartwright, J., & James, D. (2006). Frontally confined versus frontally emergent submarine landslides: A 3D seismic characterisation. *Marine and Petroleum Geology*, *23*(5), 585–604. https://doi.org/10.1016/j.marpetgeo.2006.04.002

Haflidason, H., Sejrup, H. P., Nygard, A., Mienert, J., Bryn, P., Lien, R., et al. (2004). The Storegga slide: Architecture, geometry and slide development. *Marine Geology*, *213*(1–4), 201–234. https://doi.org/10.1016/j.margeo.2004.10.007

Imran, J., Harff, P., & Parker, G. (2001). A numerical model of submarine debris flow with graphical user interface. *Computers & Geosciences*, *27*(6), 717–729. https://doi.org/10.1016/s0098-3004(00)00124-2

Issler, D., L'Heureux, J. S., Cepeda, J. M., & Quan Luna, B. (2015). Towards a numerical run-out model for quick-clay slides. In *EGU general assembly 2015*.

Kim, J., Løvholt, F., Issler, D., & Forsberg, C. F. (2019). Landslide material control on tsunami Genesis—The Storegga slide and tsunami (8, 100 years BP). *Journal of Geophysical Research: Oceans*, *124*(6), 3607–3627. https://doi.org/10.1029/2018jc014893

Klein, B., & Puzrin, A. M. (2021). Growth of slip surfaces in 3D conical slopes. *International Journal for Numerical and Analytical Methods in Geomechanics*, *45*(12), 1683–1711. https://doi.org/10.1002/nag.3220

Kvalstad, T. J., Andresen, L., Forsberg, C. F., Berg, K., Bryn, P., & Wangen, M. (2005). The Storegga slide: Evaluation of triggering sources and slide mechanics. *Marine and Petroleum Geology*, *22*(1–2), 245–256. https://doi.org/10.1016/j.marpetgeo.2004.10.019

L'Heureux, J. S., Longva, O., Steiner, A., Hansen, L., Vardy, M. E., Vanneste, M., et al. (2012). Identification of weak layers and their role for stability of slopes at Finneidfjord, Northern Norway. In Y. Yamada (Eds.) *Submarine mass movements and their consequences*. In *Advances in natural and technological hazards research* (Vol. 31). Springer.

Lin, C. H., Kumagai, H., Ando, M., & Shin, T. C. (2010). Detection of landslides and submarine slumps using broadband seismic networks. *Geophysical Research Letters*, *37*(22), L22309. https://doi.org/10.1029/2010gl044685

Locat, J., Leroueil, S., Locat, A., & Lee, H. (2014). Weak layers: Their definition and classification from a geotechnical perspective. In *Submarine mass movements and their consequences* (pp. 3–12). Springer.

Masson, D. G., Harbitz, C. B., Wynn, R. B., Pedersen, G., & Løvholt, F. (2006). Submarine landslides: Processes, triggers and hazard prediction. *Philosophical Transactions of the Royal Society A: Mathematical, Physical & Engineering Sciences*, *364*(1845), 2009–2039. https://doi.org/10.1098/rsta.2006.1810

Micallef, A., Masson, D. G., Berndt, C., & Stow, D. A. V. (2007). Morphology and mechanics of submarine spreading: A case study from the Storegga slide. *Journal of Geophysical Research*, *112*(F3), F03023. https://doi.org/10.1029/2006jf000739

Morgenstern, N., & Price, V. (1965). The analysis of the stability of general slip surfaces. *Géotechnique*, *15*(1), 79–93. https://doi.org/10.1680/geot.1965.15.1.79

Norem, H., Locat, J., & Schieldrop, B. (1990). An approach to the physics and the modelling of submarine flowslides. *Marine Georesources & Geotechnology*, *9*(2), 93–111. https://doi.org/10.1080/10641199009388233

Puzrin, A. M., Germanovich, L. N., & Kim, S. (2004). Catastrophic failure of submerged slopes in normally consolidated sediments. *Géotechnique*, *54*(10), 631–643. https://doi.org/10.1680/geot.54.10.631.56348

Puzrin, A. M., Gray, T. E., & Hill, A. J. (2015). Significance of the actual nonlinear slope geometry for catastrophic failure in submarine landslides. *Proceedings of the Royal Society A: Mathematical, Physical & Engineering Sciences*, *471*(2175), 20140772. https://doi.org/10.1098/rspa.2014.0772

Skempton, A. W. (1985). Residual strength of clays in landslides, folded strata and the laboratory. *Géotechnique*, *35*(1), 3–18. https://doi.org/10.1680/geot.1985.35.1.3

Somphong, C., Suppasri, A., Pakoksung, K., Nagasawa, T., Narita, Y., Tawatari, R., et al. (2022). Submarine landslide source modeling using the 3D slope stability analysis method for the 2018 Palu, Sulawesi, tsunami. *Natural Hazards and Earth System Sciences*, *22*(3), 891–907. https://doi.org/10.5194/nhess-22-891-2022

Spencer, E. (1967). A method of analysis of stability of embankments assuming parallel inter-slice forces. *Géotechnique*, *17*(1), 11–26. https://doi.org/10.1680/geot.1967.17.1.11

Sultan, N., Gaudin, M., Berne, S., Canals, M., Urgeles, R., & Lafuerza, S. (2007). Analysis of slope failures in submarine canyon heads: An example from the gulf of lions. *Journal of Geophysical Research*, *112*(F1), F01009. https://doi.org/10.1029/2005jf000408

Tappin, D. R., Matsumoto, T., Watts, P., Satake, K., McMurtry, G. M., Matsuyama, M., et al. (1999). Sediment slump likely caused 1998 Papua New Guinea tsunami. *Eos, Transactions American Geophysical Union*, *80*(30), 329–340. https://doi.org/10.1029/99eo00241

Watson, S. J., Mountjoy, J. J., & Crutchley, G. J. (2020). Tectonic and geomorphic controls on the distribution of submarine landslides across active and passive margins, eastern New Zealand. *Geological Society*, *500*(1), 477–494. https://doi.org/10.1144/sp500-2019-165

Zhang, W., Klein, B., Randolph, M. F., & Puzrin, A. M. (2021). Upslope failure mechanisms and criteria in submarine landslides: Shear band propagation, slab failure and retrogression. *Journal of Geophysical Research: Solid Earth*, *126*(9), e2021JB022041. https://doi.org/10.1029/2021jb022041

Zhang, W., & Puzrin, A. M. (2021). Depth integrated modelling of submarine landslide evolution. *Landslides*, *18*(9), 3063–3084. https://doi.org/10.1007/s10346-021-01655-z

Zhang, W., & Randolph, M. F. (2020). A smoothed particle hydrodynamics modelling of soil–water mixing and resulting changes in average strength. *International Journal for Numerical and Analytical Methods in Geomechanics*, *44*(11), 1548–1569. https://doi.org/10.1002/nag.3077

Zhang, W., Randolph, M. F., Puzrin, A. M., & Wang, D. (2020). Criteria for planar shear band propagation in submarine landslide along weak layers. *Landslides*, *17*(4), 855–876. https://doi.org/10.1007/s10346-019-01310-8

Zhang, W., Wang, D., Randolph, M. F., & Puzrin, A. M. (2015). Catastrophic failure in planar landslides with a fully softened weak zone. *Géotechnique*, *65*(9), 755–769. https://doi.org/10.1680/geot14.p.218

Zhang, W., Wang, D., Randolph, M. F., & Puzrin, A. M. (2016). Dynamic propagation criteria for catastrophic failure in planar landslides. *International Journal for Numerical and Analytical Methods in Geomechanics*, *40*(17), 2312–2338. https://doi.org/10.1002/nag.2531